JEM Journal of Experimental Medicine

ARTICLE

Dual role of vascular endothelial growth factor-C in post-stroke recovery

Yun Hwa Choi[1,2], Martin Hsu[3*], Collin Laaker[4*], Jenna Port[5], Kristóf G. Kovács[5], Melinda Herbath[5], Heeyoon Yang[6], Peter Cismaru[5], Alexis M. Johnson[5], Bailey Spellman[5], Kelsey Wigand[5], Matyas Sandor[5], and Zsuzsanna Fabry[5]

Cerebrospinal fluid (CSF), antigens, and antigen-presenting cells drain from the central nervous system (CNS) into lymphatic vessels near the cribriform plate and dura, yet the role of these vessels during stroke is unclear. Using a mouse model of ischemic stroke, transient middle cerebral artery occlusion (tMCAO), we demonstrate stroke-induced lymphangiogenesis near the cribriform plate, peaking at day 7 and regressing by day 14. Lymphangiogenesis is restricted to the cribriform plate and deep cervical lymph nodes and is regulated by VEGF-C/VEGFR-3 signaling. The use of a VEGFR-3 inhibitor prevented lymphangiogenesis and led to improved stroke outcomes at earlier time points, with no effects at later time points. VEGF-C delivery after tMCAO did not further increase post-stroke lymphangiogenesis, but instead induced larger brain infarcts. Our data support the damaging role of VEGF-C acutely and a pro-angiogenic role chronically. This nuanced understanding of VEGFR-3 and VEGF-C in stroke pathology advises caution regarding therapeutic VEGF-C use in stroke.

Introduction

Stroke is the fifth leading cause of death and the leading cause of long-term disability, according to the American Heart Association (Virani et al., 2020). Currently, there is only one Food and Drug Administration–approved drug available for ischemic stroke patients, tissue plasminogen activator (tPA) (Kim, 2019; Özlüer and Avcil, 2017; Knecht et al., 2018). However, tPA is only given to about 2–6% of ischemic stroke patients due to its narrow therapeutic window and its potential risk of adverse effects such as intracerebral hemorrhagic conversion (Kim, 2019; Knecht et al., 2017, 2018; Alberts, 2017; Gravanis and Tsirka, 2008; Lin et al., 2018; Barber et al., 2001; Miller et al., 2011). For years, researchers have tried to develop better therapeutic approaches for ischemic stroke, but most clinical trials have fallen short (Xu and Pan, 2013; Chen and Wang, 2016; Cheng et al., 2004; Stroke Therapy Academic Industry Roundtable II (STAIR-II), 2001).

Stroke leads to acute brain edema that contributes to blood–brain barrier disruption, inflammation, and homeostatic disbalance (Rosenberg, 1999). Resolution of brain edema has been associated with functional lymphatic clearance of the brain (Si et al., 2006; Chen et al., 2019; Hu et al., 2020). Paradoxically, both inducing lymphatic vessel formation or inhibiting lymphangiogenesis have been proposed as potential therapies for the resolution of post-stroke brain edemas and accelerating post-stroke recovery (Esposito et al., 2019; Kim et al., 2021; Boisserand et al., 2024; Keuters et al., 2024). One of the difficulties of designing lymphatic-targeting therapies in stroke lies in the uncertainty of the targeted pathways or exact mechanisms. Different lymphatic vessels around the brain could mediate lymphatic clearance, including the dural meningeal lymphatics (Da Mesquita et al., 2018; Wen et al., 2018), basal lymphatics (Ahn et al., 2019), and the cribriform plate (CP) lymphatics (Hsu et al., 2019). These lymphatic vessels have been shown to be involved in transporting fluid, waste, and immune cells in a variety of pathological states (Alitalo, 2011; Ma et al., 2017). Previously, our lab has shown that lymphatic vessels near the CP proliferate and expand in experimental autoimmune encephalomyelitis, a mouse model of autoimmune-mediated neuroinflammation. These newly formed lymphatic vessels have immunoregulatory functions that may manage neuroinflammatory diseases (Hsu et al., 2019, 2022). Intriguingly, it was reported that stroke induces lymphangiogenesis at the dural meningeal lymphatics in mouse intracerebral hemorrhage (Tsai et al., 2022) and photothrombosis mouse stroke models (Yanev et al., 2020); however, whether targeting these pathways would be beneficial for stroke recovery is still unknown.

[1]Department of Medicine, University of Wisconsin-Madison, Madison, WI, USA; [2]Waisman Center, University of Wisconsin-Madison, Madison, WI, USA; [3]Department of Microbiology and Immunology, University of North Carolina, Chapel Hill, Chapel Hill, NC, USA; [4]Neuroscience Training Program, University of Wisconsin-Madison, Madison, WI, USA; [5]Department of Pathology and Laboratory Medicine, University of Wisconsin-Madison, Madison, WI, USA; [6]College of Agricultural and Life Sciences, University of Wisconsin-Madison, Madison, WI, USA.

*M. Hsu and C. Laaker contributed equally to this paper. Correspondence to Zsuzsanna Fabry: zfabry@wisc.edu.

Manipulating the vascular endothelial growth factor receptor 3/vascular endothelial growth factor-C (VEGFR-3/VEGF-C)–mediated lymphangiogenesis pathway has been proposed as a potential therapy for stroke treatment (Esposito et al., 2019; Yanev et al., 2020; Tsai et al., 2022; Boisserand et al., 2024; Keuters et al., 2024). VEGF-C is commonly secreted by immune cells during inflammatory events and binds to VEGFR-3 expressed on lymphatic vessels to stimulate lymphangiogenesis (Flister et al., 2010). VEGF-C has been documented to increase in the central nervous system (CNS) in days following stroke (Gu et al., 2001; Shin et al., 2008; Bain et al., 2013). However, the contribution of VEGFR-3/VEGF-C signaling to stroke pathology still remains controversial. Some reports indicate VEGF-C may improve post-stroke recovery by promoting the survival of neural stem cells (Matta et al., 2021) or promoting increases in CNS clearance through expansion of dural meningeal lymphatic vessels (Tsai et al., 2022). Conversely, others have suggested that early widespread blockade of VEGFR-3 and VEGF-C signaling can reduce ischemic infarction size through reductions in pro-inflammatory immune activation within the cervical lymph nodes (Esposito et al., 2019) and counteracting the chemotactic effect of VEGF-C (Shin et al., 2008).

To clarify the role of lymphatics in post-stroke pathology, we investigated the impact of ischemic stroke in multiple CNS-associated lymphatic regions (CP, dura, and basal), and deep cervical lymph nodes (dCLNs) and tested the effects of VEGFR-3/VEGF-C signaling on stroke outcome. Using a transient middle cerebral artery occlusion (tMCAO) mouse model, we found that after 3 days of tMCAO, lymphangiogenesis occurs near the CP, which peaked at day 7 and returns to baseline by day 14. We did not see evidence for lymphangiogenesis at the dural lymphatic vasculature. Cranial dural meningeal lymphatics adapted to stroke-induced neuroinflammation by dilation 3 days following tMCAO. Lymphatic expansion at the CP was associated with increased interaction between lymphatic endothelial and immune cells, particularly with macrophages and dendritic cells (DCs). VEGF-C–secreting myeloid cells, including DCs, were bound to the CP lymphatics, and lymphangiogenesis was inhibited with the VEGFR-3 blocker MAZ51. We show significant fluid drainage through the newly formed lymphatic vessels during the peak of lymphangiogenesis at the CP in parallel with increased lymphangiogenesis at the downstream CNS-draining cervical lymph nodes. We did not find increased lymphangiogenesis at the distant axillary, inguinal, and popliteal lymph nodes after stroke. Confirming the therapeutic findings by others (Esposito et al., 2019), inhibition of VEGFR-3 signaling not only blocked lymphangiogenesis near the CP and dilation of cranial dural LVs but also led to smaller brain infarcts and improved motor functions following tMCAO. With the goal of increasing stroke neuroinflammation-induced drainage of the brain, we administered VEGF-C156S through the left common carotid artery (CCA) after tMCAO. However, post-stroke VEGF-C treatment induced larger brain infarcts without further inducing changes in lymphatics in the cranial dura and CP lymphatics. Our data support that VEGF-C has a dual role in stroke, exacerbating damage in the acute phase and promoting lymphangiogenesis in the chronic phase of stroke. Furthermore, despite a VEGFR-3–dependent induction of lymphangiogenesis near the CP after ischemic stroke in mice, therapeutic targeting of these VEGF-C/VEGFR-3 interactions for stroke therapy should be cautioned.

Results

CP lymphatics undergo lymphangiogenesis after stroke

We first looked to confirm if lymphangiogenesis occurs in cribriform plate lymphatic vessels (cpLVs) after tMCAO. Our lab previously showed that lymphangiogenesis occurs at the CP in the experimental autoimmune encephalomyelitis model of autoimmune-mediated neuroinflammation (Hsu et al., 2019). After inducing tMCAO for 60 min in wild-type male mice, stroke lesion size was measured using T2-weighted magnetic resonance imaging (MRI), and then mice were sacrificed on day 3, 7, or 14. Additionally, at each time point, whole heads were fixed, decalcified, and then sectioned for immunohistochemistry (IHC) of the CP–olfactory region, staining for lymphatic vessel endothelial hyaluronan receptor 1 (Lyve-1) fluorescent antibody to identify lymphatic vessels at each time point (Fig. 1 A). Coronal sections allow for visualization of Lyve-1$^+$ cpLVs extending above the CP positioned between the olfactory bulbs (OB) in mice (Fig. 1 B). Brain infarction was confirmed at all time points in sham and tMCAO groups. Infarction areas were calculated to be between 30 and 40% across days 3, 7, and 14 with slightly lower percentages at day 14 after tMCAO (Fig. 1 C). Average Lyve-1$^+$ vessel areas were significantly elevated at day 3, peaking at day 7, and then decreased at day 14 in the tMCAO group, while the sham group did not show changes across those time points (Fig. 1 D). Lymphatic loops and sprouts morphology are a measurement of increased complexity and can be used to estimate lymphatic proliferation or lymphangiogenesis (Kajiya et al., 2009). The number of loops was increased at the CP among tMCAO groups at both days 3 and 7, while the number of sprouts was increased at days 3, 7, and 14 (Fig. 1 E). We also measured the length of cpLVs starting from the nasal mucosa to the tip of the lymphatic vessels between the OB. The lengths were increased at days 3 and 7, and then decreased to similar lengths of sham groups at day 14 (Fig. 1 E). These data indicate that lymphangiogenesis near the CP occurs and initiates around day 3 and regresses by day 14 after tMCAO.

We tested whether other lymphatic regions also undergo lymphangiogenesis after tMCAO. We first investigated basal lymphatic regions near the optic nerve and nasopharynx (NP), which are proposed to integrate with cribriform lymphatic pathways (Yoon et al., 2024; Antila et al., 2024), but we did not detect increases in Lyve-1 area at any time point after tMCAO (Fig. S1, A and B). Additionally, we investigated meningeal lymphatics in the dura above the brain and tested if they underwent changes after tMCAO. We show that average Lyve-1$^+$ vessel areas of the confluence of sinuses (COS) of dural lymphatics were increased at days 3 and 7 and then returned to baseline level by day 14 after tMCAO compared with sham groups (Fig. S1 C). When we looked at the superior sagittal sinus (SSS) of the dural lymphatics, there was an increase in Lyve-1$^+$

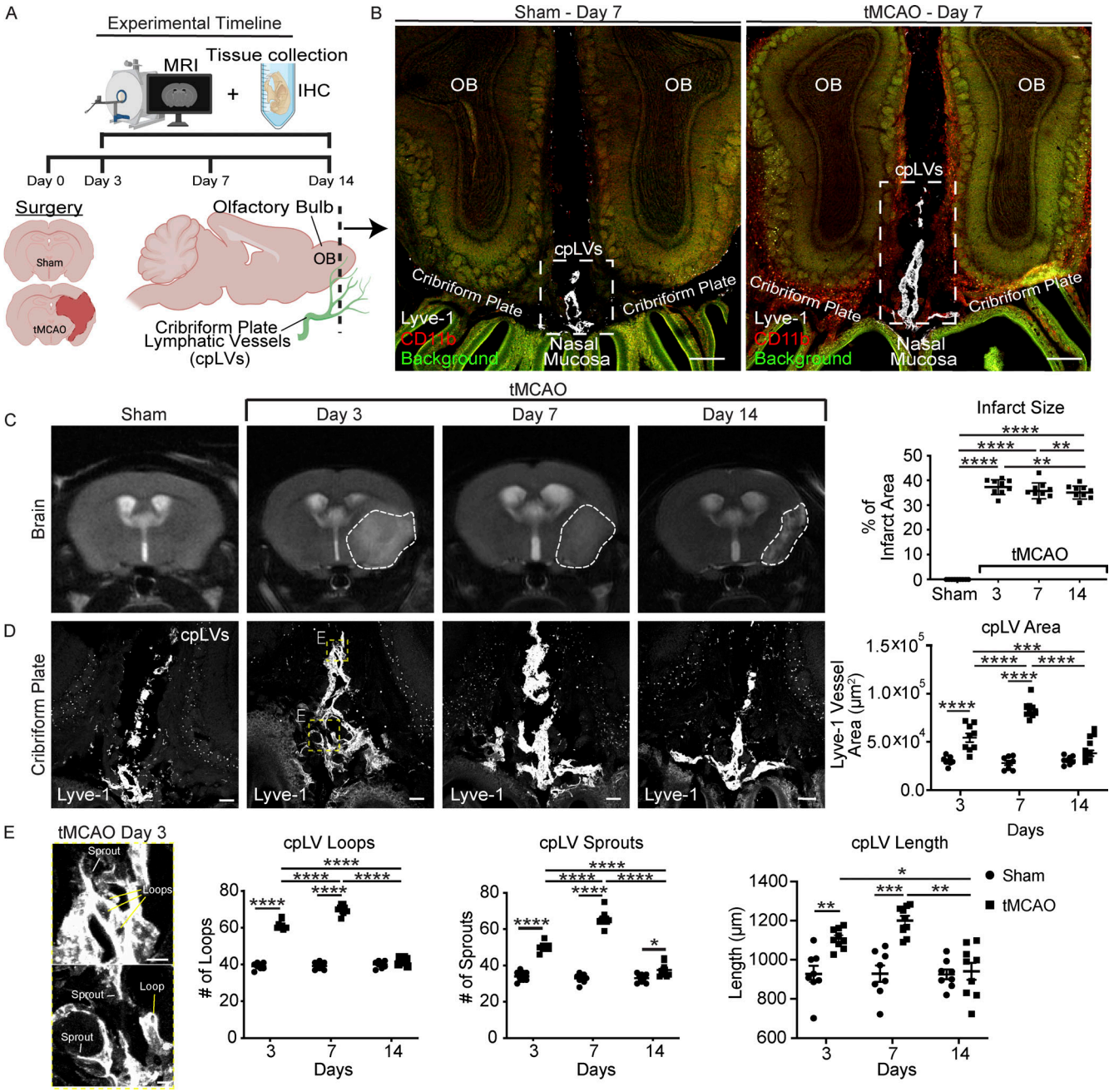

Figure 1. **tMCAO induces lymphangiogenesis at the CP lymphatic vasculature. (A)** Experimental timeline. Sham and 60-min tMCAO surgeries were performed on 10–12-wk-old male mice (25–29 g). Across three time points (days 3, 7, and 14), T2-weighted MRIs of the infarct area and multiple tissue regions were collected for lymphatic analysis of the CP, optic nerve, NP, dura, and lymph nodes (created using https://BioRender.com). **(B)** Representative images to demonstrate the position of Lyve-1⁺ cpLVs which are positioned between OB from a sham and tMCAO mouse on day 7 after surgery. Sections were stained with CD11b (red) to visualize myeloid cells and Lyve-1 (white) to visualize cpLVs. Dotted boxes outline Lyve-1⁺ cpLVs. Scale bars = 300 μm. **(C)** T2-weighted MRI images of brain sections between sham and tMCAO at days 3, 7, and 14. Representative images of MRI brain scans after sham and tMCAO. White dashed lines mark brain infarcts, which are quantified into a graph (n = 8 mice for sham, n = 9 mice for tMCAO; mean ± SEM, **P ≤ 0.01, ****P ≤ 0.0001, two-way ANOVA). **(D)** 60-μm coronal sections of CP areas were immunolabeled for Lyve-1 to visualize lymphatic vessels after 3, 7, and 14 days of sham or tMCAO and quantified. Representative confocal images of lymphatic vessels near the CP. Quantitation of average Lyve-1⁺ vessel area near the CP (n = 8 mice for sham, n = 9 mice for tMCAO; mean ± SEM, ***P ≤ 0.001, ****P ≤0.0001, two-way ANOVA). Scale bars = 100 μm. **(E)** Quantitation of number of lymphatic loops, sprouts (see representative image, day 3 tMCAO) and length near the CP after sham and tMCAO at days 3, 7, and 14 (n = 8 mice for sham, n = 9 mice for tMCAO; mean ± SEM, *P ≤ 0.05, **P ≤ 0.01, ***P ≤ 0.001, ****P ≤ 0.0001, two-way ANOVA). Scale bars = 20 μm. Source data are available for this figure: SourceData F1.

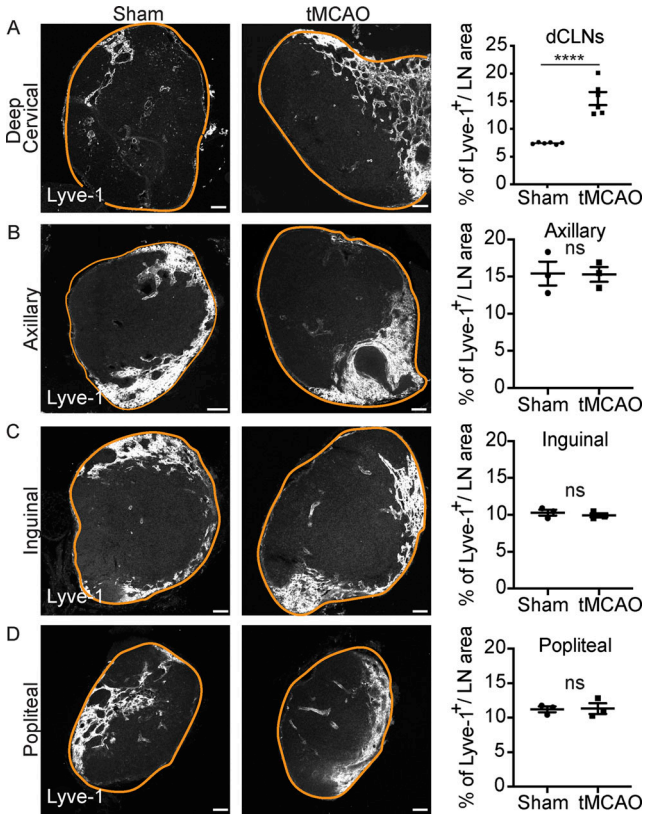

Figure 2. **dCLN lymphatics expand after tMCAO. (A–D)** Sections of dCLNs (A) and peripheral lymph nodes such as axillary (B), inguinal (C), and popliteal (D) were immunolabeled with Lyve-1 fluorescent antibody after 7 days of sham and tMCAO. Representative confocal images of each lymph node with orange lines to define the areas of lymph nodes. Scale bars = 100 µm. Quantitation of percentage of Lyve-1$^+$ vessel area over lymph node areas (n = 6 mice per group for cervical lymph nodes, n = 3 mice per group for axillary, inguinal, and popliteal lymph nodes; mean ± SEM, ****P ≤ 0.0001, unpaired Student's t test). Source data are available for this figure: SourceData F2.

vessel areas at day 7, which decreased by day 14 after tMCAO (Fig. S1 E). In order to differentiate between lymphangiogenesis associated with loop and sprout formation or dilation of lymphatic vasculature, we quantified the number of loops and sprouts of both COS and SSS in dural meningeal lymphatics, but there were no differences in both regions between sham and tMCAO groups (Fig. S1, D and F). Quantitation of lymphatic diameter in the COS showed increases at days 3 and 7 and regressed back to a similar diameter of sham groups at day 14 (Fig. S1 D). The diameter of vessels in the SSS showed increases at day 7 of tMCAO compared to sham (Fig. S1 F). Together, these data indicate that cranial dural meningeal lymphatics dilate after stroke but did not have the morphological characteristics of lymphangiogenesis as seen in the CP.

We also tested whether lymphangiogenesis extended to the peripheral lymph nodes following stroke. Increased Lyve-1$^+$ areas were observed in dCLNs 7 days following tMCAO (Fig. 2 A); however, these changes were specific to the dCLNs, since other peripheral lymph nodes such as axillary, inguinal, and popliteal had no changes in Lyve-1 area during the observation period (Fig. 2, B–D). These data support the strong regional cooperation of adaptive lymphatic responses restricted to the cervical lymphatics and the CP lymphatic vasculature.

Increased cerebrospinal fluid (CSF) accumulation at the CP lymphatics after stroke

Fluid drainage is a critical function of lymphatic vessels (Petrova and Koh, 2020), and cerebral edema is a common complication following ischemic stroke (Brogan and Manno, 2015). To test fluid drainage following tMCAO, we used T1-weighted MRI to confirm if expanded CP lymphatics can transport CSF after 7 days of tMCAO by administering gadolinium into the cisterna magna after taking baseline scans. On the dorsal view, we observed an increase in accumulation of gadolinium near the OB directly adjacent to the CP (Fig. 3, A–C). Additionally, when we injected 10 µl of 10% Evans blue dye into the cisterna magna of tMCAO mice, the Evans blue dye in the coronal sections of CP regions co-localized with Lyve-1$^+$ lymphatic vessels (Fig. S2, A–C) and around olfactory nerves (Fig. S2 D). Representative fluorescent intensity profile plot of Evans blue dye and Lyve-1 from a cross-section of the merged image confirmed cpLV co-localization (dotted line) (Fig. S2 C). Together, these data suggest that CSF can be drained through lymphangiogenic vessels after tMCAO.

CP lymphatics interact with VEGF-C–producing myeloid cells after tMCAO

The induction of lymphangiogenesis occurs via the interaction of secreted VEGF-C binding to VEGFR-3 receptors expressed on lymphatic endothelial cells (LECs) (Kajiya et al., 2009; Yan et al., 2017; Aspelund et al., 2014). To test whether VEGF-C is elevated near the CP lymphatics following tMCAO, we collected decalcified CPs from both sham and tMCAO groups and stained for VEGF-C at 7 days after surgery. While we found some evidence of VEGF-C expression near cpLVs in sham animals (Fig. 4 A), VEGF-C in Lyve-1 regions was increased significantly during tMCAO with VEGFC$^+$ cells binding directly to cpLVs (Fig. 4, B and C; yellow arrowheads).

Previously we have shown that autoimmune inflammation of the CNS induces higher adhesion molecule expression on cribriform plate lymphatic endothelial cells (cpLECs) and retention of recruited VEGF-C–producing immune cells at these vessels (Hsu et al., 2022). We hypothesized cpLECs were also interacting with immune cells after stroke, and we investigated cell–cell interactions by analyzing doublets within the flow cytometry dataset (Halpern et al., 2018; Giladi et al., 2020; Bendall, 2020; Hsu et al., 2022). We studied the doublets forming between leukocytes and cpLECs 7 days following tMCAO by gating for LECs (CD31$^+$, podoplanin [PDPN]$^+$) within CD45$^+$ clusters and then further gating for macrophage (CD45^{hi}, CD11b$^+$, and CD11c$^-$), DCs (CD45^{hi}, CD11b$^+$, and CD11c$^+$), CD8 T cells (CD45^{hi}, CD11b$^-$, CD11c$^-$, and CD8$^+$), CD4 T cells (CD45^{hi}, CD11b$^-$, CD11c$^-$, and CD4$^+$), and B cells (CD45^{hi}, CD11b$^-$, CD11c$^-$, CD8$^-$, CD4$^-$, and B220$^+$) in both sham and tMCAO groups (Fig. 4 D). We found that the number of CD31$^+$, PDPN$^+$ cells, which we identified as cpLECs in doublets, was increased in tMCAO groups as well as macrophages and DCs (Fig. 4 E). IHC confirmed that DCs and macrophages are bound directly to cpLVs following stroke orthogonal view of a CP section showed that Lyve-1$^+$ lymphatics

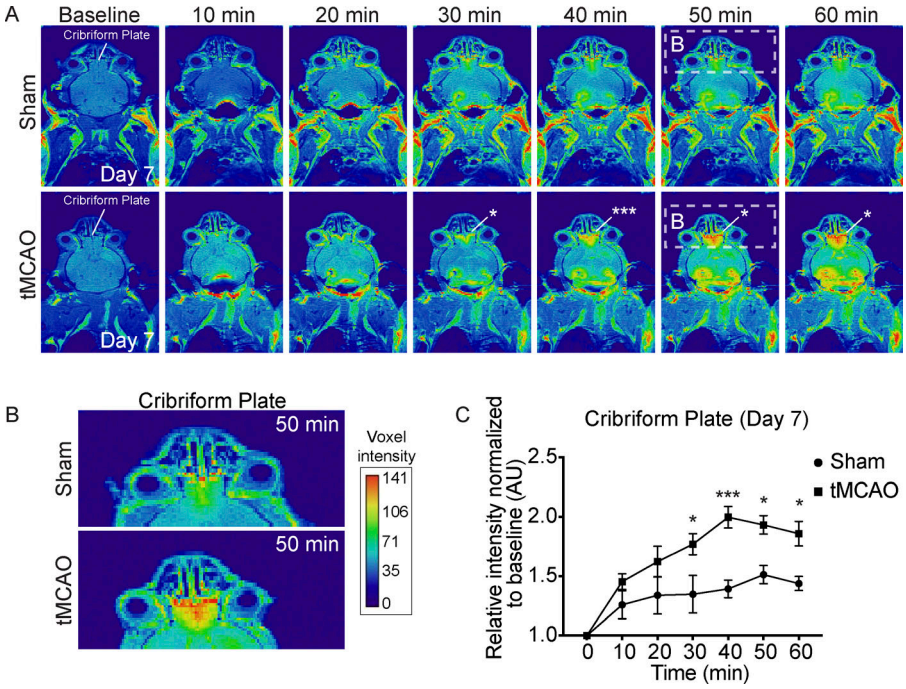

Figure 3. **tMCAO induces CSF accumulation at the CP lymphatics. (A and B)** Representative T1-weighted MRI scan images of dorsal (A) and view of mice whole heads between sham and tMCAO 7 days after surgery. Baseline images were imaged before gadolinium injection and serial images over time were imaged after injection. **(B)** Zoomed representative image from 50-min time point shows increased signal intensity at CP region. **(C)** Quantitation of average pixel intensity normalized to baseline of the CP between sham and tMCAO mice (n = 3 mice for sham, n = 5 mice for tMCAO; mean ± SEM, *P ≤ 0.05, ***P ≤ 0.001, two-way ANOVA with repeated measures). Source data are available for this figure: SourceData F3.

near the CP are in close contact with CD11b$^+$ and CD11c^{high} DCs (Fig. 4 F). To determine if lymphatic-interacting macrophages and DCs were local sources of VEGF-C following stroke, we analyzed sections of CP areas stained using fluorescent-labeled antibodies of Lyve-1, CD11b, CD11c, and VEGF-C. VEGF-C–expressing CD11b$^+$ cells aggregated near the CP lymphatics after 7 days of tMCAO in mice (Fig. 4 G). Additionally, we observed VEGF-C–expressing CD11b^{high}, CD11c$^+$ and CD11b^{low}, CD11c$^+$ near the CP (Fig. 4 G). Together, these data show that VEGF-C is increased at the CP following tMCAO with lymphatic-interacting macrophages and DCs providing a local source of VEGF-C at this site after 7 days of tMCAO.

VEGFR-3 inhibition reduces brain infarct and improves early motor recovery after tMCAO

To understand the role of VEGFR-3/VEGF-C interaction in the outcome of tMCAO, we used a VEGFR-3 tyrosine kinase inhibitor, MAZ51, to inhibit pro-lymphangiogenic signaling and to assess potential therapeutic effects (Kirkin et al., 2001, 2004). Either DMSO (solvent control of MAZ51) or MAZ51 was administered i.p. on days 0, 2, 4, and 6 to control groups and experimental groups (Fig. 5 A). Average Lyve-1$^+$ vessel areas near the CP were reduced after MAZ51 treatment in tMCAO groups, while MAZ51 did not induce further regression of lymphatics in sham groups (Fig. 5, B and C). The COS and SSS of dural meningeal lymphatics showed decreased Lyve-1 area after MAZ51 in tMCAO groups (Fig. S3, A and B). Similarly, lymphatics in the dCLNs showed regression of Lyve-1$^+$ vessels after MAZ51 treatment (Fig. S3 C). These data confirm that post-stroke lymphangiogenesis occurs at the CP via the interaction of VEGF-C and VEGFR-3.

To test the role of CP lymphangiogenesis in the pathological outcomes following stroke, we performed T2-weighted MRI imaging to measure brain infarction following i.p. administration of MAZ51. Interestingly, 7 days following tMCAO, MAZ51-treated mice showed decreased infarction areas compared with control-treated tMCAO mice (Fig. 5, D and E). During MAZ51 treatments the ladder rung test, open-field, and rotarod, were also conducted on days 1, 3, 5, and 7 after sham or tMCAO to test motor function (Fig. S4 A). On the ladder rung test, MAZ51-treated tMCAO mice showed improvements by making less foot faults starting from day 3 compared with control-treated tMCAO mice (Fig. S4 B). In the open-field tests, each mouse was placed in the center of the box, and their movements were tracked. Broadly, failure to exit the center zone after initial placement was associated with motor impairment in the open-field test (Skillings et al., 2014), as tMCAO mice exhibited "circling behavior" due to single-side paralysis (Ruan and Yao, 2020) and were unable to travel in a straight line toward the peripheral wall (Fig. S4 C). Quantification of the latency to exit the center zone of the box showed that MAZ51-treated tMCAO mice were quicker to leave the center compared to control-treated tMCAO mice on day 1 (Fig. S4, D and E). In the rotarod test, control-treated tMCAO mice showed improvements at day 7, while MAZ51-treated tMCAO mice did not (Fig. S4 F). In summary, MAZ51-treated tMCAO mice showed better locomotor ability in ladder rung tests and open-field tests as well as reduced brain infarct areas, starting from as early as day 1. However, these MAZ51-treated tMCAO mice showed hindered natural recovery along with worse coordination and balance at day 7 in rotarod tests. This result correlates with regressed lymphangiogenesis near the CP and lymphatic dilation of dural meningeal lymphatics after MAZ51 treatment (Fig. S4 G).

Immediate VEGF-C delivery locally to the lesion after tMCAO does not further elevate CP lymphangiogenesis, but worsens brain infarct

VEGF-C administration has been proposed to diminish brain edema, increase brain drainage, and promote regeneration

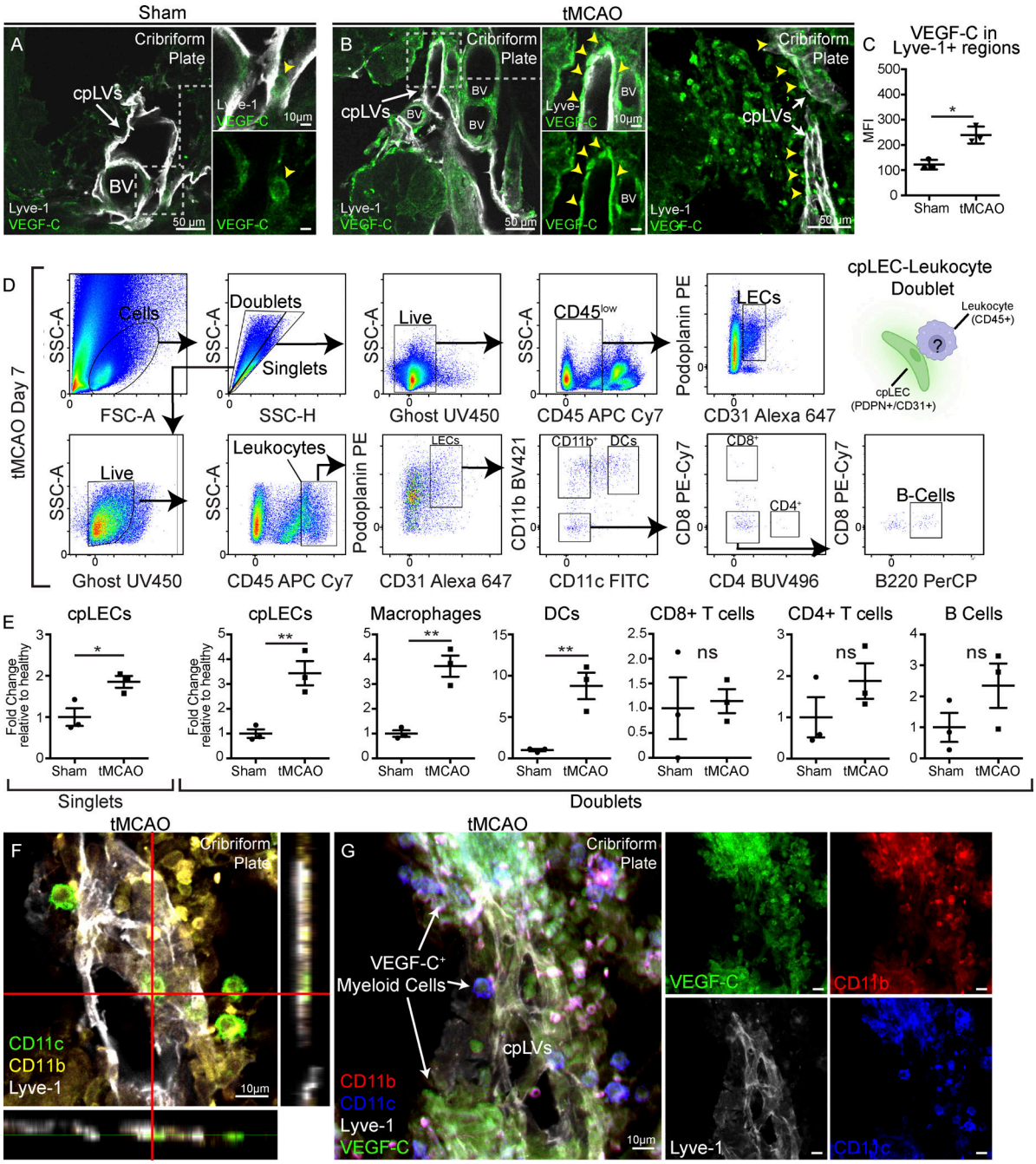

Figure 4. **VEGF-C–producing myeloid cells interact with cpLVs after tMCAO. (A–C)** CP sections from sham (A) and tMCAO (B) mice were stained with VEGF-C and Lyve-1 antibodies 7 days after surgery (peak lymphangiogenesis). VEGF-C$^+$ cells were observed near Lyve-1$^+$ vasculature in sham and tMCAO mice (yellow arrowheads). VEGF-C fluorescence within Lyve-1$^+$ cpLVs was measured between groups. Mean fluorescent intensity (MFI) of VEGF-C in Lyve-1$^+$ regions were quantified (C) (n = 3 mice per group; mean ± SEM, *P < 0.05, unpaired Student's t test). Scale bars = 50 µm, 10 µm. **(D)** Cell-to-cell interactions between cpLECs and immune cells were studied by gating for live doublets from the CP cell suspensions. cpLECs were gated as doublets, live, and CD45$^+$, CD31$^+$, and PDPN$^+$. Macrophages were gated as CD45^{hi}, CD11b$^+$, and CD11c$^-$. DCs were gated as CD45^{hi}, CD11b$^+$, and CD11c$^+$. CD4 T cells were gated as CD45^{hi}, CD11b$^-$, CD11c$^-$, and CD4$^+$. CD8 T cells were gated as CD45^{hi}, CD11b$^-$, CD11c$^-$, and CD8$^+$. B cells were gated as CD45^{hi}, CD11b$^-$, CD11c$^-$, CD4$^-$, CD8$^-$, and B220$^+$. cpLECs from singlets were gated as singlets, live, and CD45$^-$, CD31$^+$, and PDPN$^+$. **(E)** Quantitation of number of cpLECs in singlets, number of cpLECs in doublets, and number of immune cells in doublets near the CP between sham and tMCAO groups after 7 days. Values presented as fold change normalized relative to healthy (n = 3 mice per group; mean ± SEM, *P < 0.05, **P ≤ 0.01, unpaired Student's t test). **(F)** Representative orthogonal sectional view of CP after 7 days of tMCAO showing CD11b$^+$, CD11c$^+$ DCs are bound to Lyve-1$^+$ lymphatic vessels. Scale bar = 10 µm. **(G)** Representative sectional images of CP areas after immunolabeling with CD11b, CD11c, VEGF-C, and Lyve-1 to visualize immune cells and lymphatic vessels after 7 days of sham and tMCAO. Scale bars = 10 µm. BV = blood vessels. Source data are available for this figure: SourceData F4.

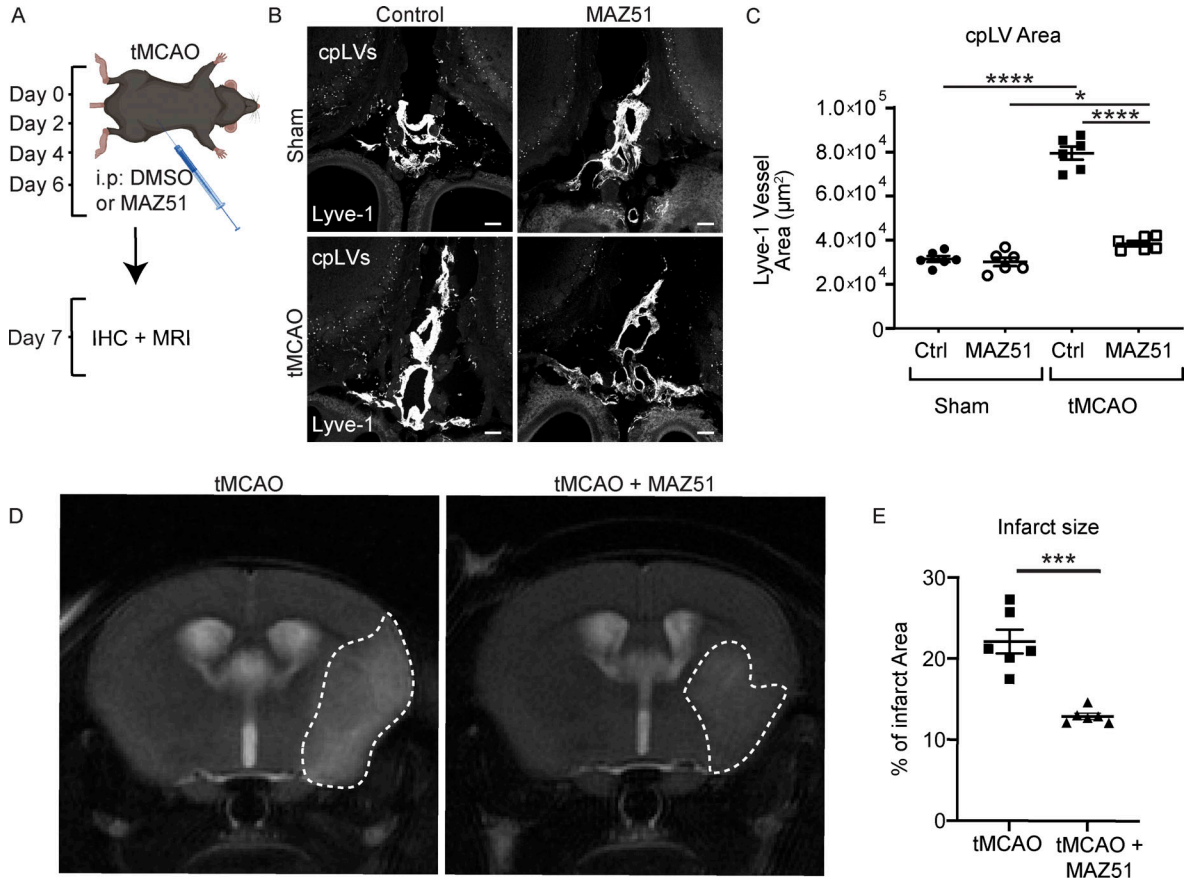

Figure 5. **MAZ51 blocks post-stroke cpLV vessel expansion and reduces brain infarct size. (A)** Experimental design for administering i.p. injection of DMSO or MAZ51 (VEGFR-3 inhibitor) after reperfusion of tMCAO (day 0). MRI and tissue collection were acquired on day 7 after tMCAO (created using https://BioRender.com). **(B and C)** Coronal sections of CP areas were stained with Lyve-1 fluorescent antibody after either control or MAZ51 treatment in sham or tMCAO mice. Representative confocal images of lymphatic vessels near the CP. Scale bars = 100 µm for CP sections (B). Quantitation of average Lyve-1⁺ vessel area near the CP at day 7 after stroke (C) (n = 6 mice per group; mean ± SEM, *P ≤ 0.05, ****P ≤ 0.0001, one-way ANOVA). **(D and E)** T2-weighted MRI scan images of brain sections between tMCAO with control or MAZ51 treatment at day 7. Representative images of MRI brain scans (D). White dashed lines mark brain infarcts which are quantified into a graph (E) (n = 6 mice per group; mean ± SEM, ***P ≤ 0.001, unpaired Student's t test). Source data are available for this figure: SourceData F5.

following neuroinflammatory damage to the brain (Tsai et al., 2022; Matta et al., 2021). To test whether this treatment would be beneficial following ischemic damage to the brain, we induced 60-min ischemia followed by reperfusion using the tMCAO model. We then administered VEGF-C156S or PBS through the CCA using a microcatheter on day 0 of the tMCAO (Fig. 6 A). VEGF-C156S specifically activates VEGFR-3, unlike endogenous forms of VEGF-C, which can also bind to VEGFR-2 (Joukov et al., 1998). Quantitation of Lyve-1⁺ vessels showed there was no further increase in lymphatic measurements near the CP, COS, and SSS of dural meningeal lymphatics, or in dCLNs after VEGF-C156S treatment (Fig. 6 B and Fig. S5). However, brain infarction was significantly increased after VEGF-C156S treatment at both days 3 and 7 compared with control-treated tMCAO mice (Fig. 6 C). To better understand the elevation of infarct size, we investigated alterations in peripheral immune cell populations as they may have been influenced by VEGF-C156S administration. Interestingly, we found that around the subfornical vessels of the brain, a commonly reported site of immune cell infiltration into the CNS (Schulz and Engelhardt, 2005; D'Mello et al., 2009), there was an increased number of CD45⁺ leukocytes in the perivascular regions of the vessels (Fig. 6 D). Together, these data suggest that post-stroke VEGF-C delivery could exacerbate stroke damage, elevate neuroinflammation, and promote immune cell aggregation at barrier sites in the brain while not directly enhancing lymphangiogenesis surrounding the CNS.

Discussion

Here we showed for the first time that lymphatic vessels near the CP undergo lymphangiogenesis after tMCAO and that these newly formed vessels drain CSF as well as retain immune cells following stroke. As ischemic areas undergo necrosis and apoptosis due to deprivation of oxygen and nutrients, pro-inflammatory cytokines and chemokines are released, which recruit immune cells to the injury site (Gesuete et al., 2016). Simultaneously, cerebral edema can occur as one of the complications of ischemic stroke (Dostovic et al., 2016). Since the brain is enclosed within the skull, increased intracranial

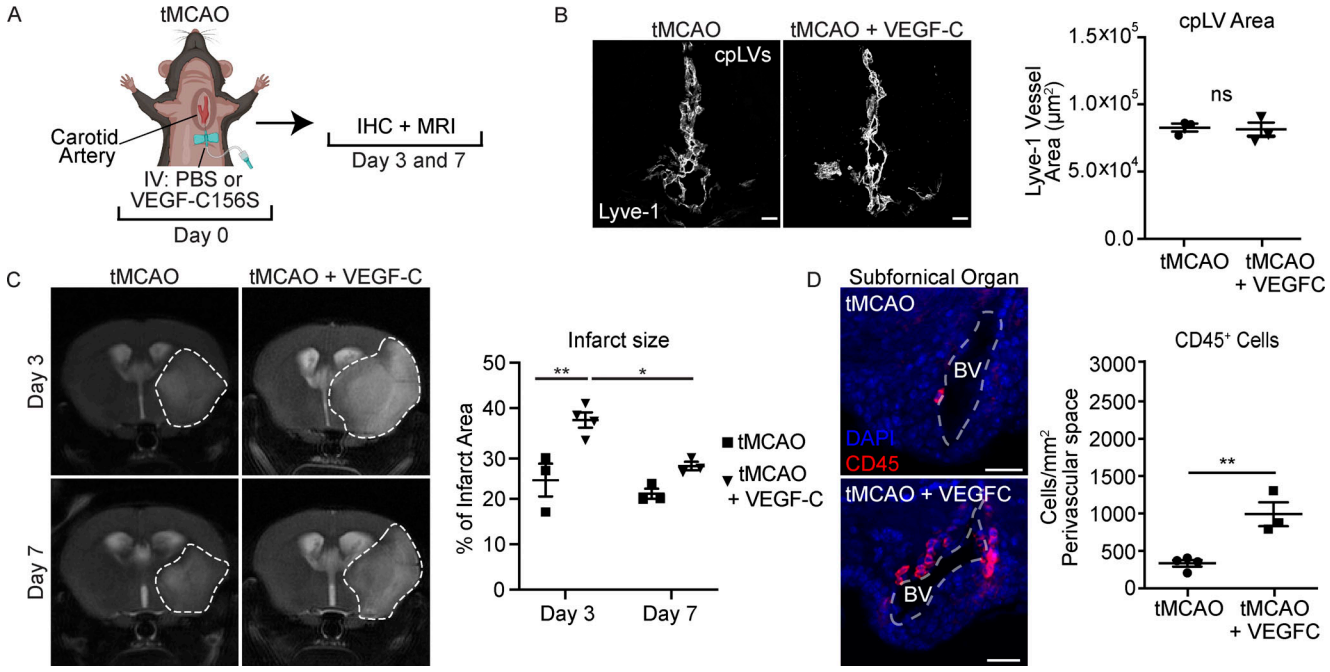

Figure 6. **Post-stroke intracatheter delivery of VEGF-C exacerbates stroke damage without inducing additional expansion of cpLVs. (A)** Experimental design for administering control or VEGF-C156S through the artery after reperfusion of tMCAO (day 0) and euthanasia at days 3 and 7 for decalcification steps (created using https://BioRender.com). **(B)** Coronal sections of CP areas were stained with Lyve-1 fluorescent antibody after either control or VEGF-C156S treatment of tMCAO mice at day 7. Representative confocal images of lymphatic vessels near the CP. Quantitation of each image (n = 3 mice per group; mean ± SEM, unpaired Student's t test). Scale bars = 100 µm. **(C)** T2-weighted MRI scanned images of brain sections between tMCAO and tMCAO with VEGF-C156S treatment at days 3 and 7. Representative images of MRI brain scans. White dashed lines mark brain infarcts, which are quantified into a graph (n = 3 mice per group, n = 4 mice for tMCAO with VEGF-C156S at day 3; mean ± SEM, *P ≤ 0.05, **P ≤ 0.0, two-way ANOVA with mixed effects). **(D)** Coronal brain sections were stained with CD45 fluorescent antibody (Alexa 647) at day 3 after tMCAO/VEGF-C treatment. Subfornical vessels near the third ventricle were analyzed for perivascular leukocyte cell number. (n = 4 mice for tMCAO, n = 3 mice for tMCAO with VEGF-C156S; mean ± SEM, **P ≤ 0.01, unpaired Student's t test). Scale bars = 20 µm. BV = blood vessel. Source data are available for this figure: SourceData F6.

pressure exerted by the brain and CSF can lead to secondary brain ischemia through the reduction of cerebral blood flow and increasing tissue hypoxia (Jeon et al., 2014). This can ultimately cause death in some stroke patients (Jeon et al., 2014; Thorén et al., 2017). As a result, efficient drainage of fluid from the CNS, especially during inflammation, is necessary to prevent the worst outcomes.

Multiple routes that drain fluid and cells in the CNS have been recharacterized recently (Engelhardt et al., 2017; Proulx, 2021; Laaker et al., 2023). However, there are still controversial debates regarding each route's contribution to the drainage of CSF, antigens, and immune cells during both steady state and neuroinflammation. Several groups have shown that lymphatics near the CP play significant roles in the drainage of CSF and cells to CLNs in animals (Hsu et al., 2019; Walter et al., 2006; Pashenkov et al., 2003; Cserr et al., 1992; Mollanji et al., 2001; Madarasz et al., 2024), but the role of this pathway in humans is still unclear with recent reports indicating no evidence of CSF outflow into the nasal mucosa (Melin et al., 2020) and others reporting clear visualization (Zhou et al., 2022). However, interestingly recent characterization of the CP lymphatics in mice has revealed discontinuity of the E-cadherin⁺ arachnoid layer at this region, potentially allowing cribriform lymphatic vessels more permissible access to fluid, antigen, and cells draining in the subarachnoid space around olfactory nerves (Spera et al., 2023; Hsu et al., 2022).

This study shows increased numbers of loops and sprouts at the CP that correlate with increased Lyve-1⁺ vessel area following stroke. The data presented here indicate that lymphangiogenesis near the CP is transient and progressive, starting at day 3, peaking at day 7, and regressing by day 14. Flow cytometry data confirmed lymphangiogenesis by showing an expansion of the number of cpLECs after tMCAO. Stroke-induced lymphangiogenesis was unique to the CP and draining cervical lymph nodes, as neither the dural meningeal lymphatics nor the distant lymph nodes showed an increase in lymphatic area and loops or sprouting. Dural meningeal lymphatics have shown an increase of diameters in response to VEGF-C, which is naturally elevated in CSF after stroke due to increased interstitial fluid pressure and lymphedema (Da Mesquita et al., 2018; Esposito et al., 2019; Gu et al., 2001; Rutkowski et al., 2006). Other groups have shown that impairment of dural meningeal lymphatics affected clearance of macromolecules, but not increased interstitial fluid pressure, which indicates there is another route contributing to removal of extra fluid in the brain during inflammation (Da Mesquita et al., 2018; Aspelund et al., 2015). We found that dCLNs experienced post-stroke lymphangiogenesis, implying that a greater connection to CNS fluid and cell drainage pathways may be necessary to drive post-stroke lymphatic vessel growth in the periphery. We show that lymphangiogenic vessels at the CP can retain immune cells,

including macrophages and DCs, after stroke. Previous data showed that neuroinflammation created an immune regulatory niche at the CP, in which LECs upregulate genes involved in leukocyte crosstalk, including those of adhesion molecules, chemokines, and antigen presentation (Hsu et al., 2022). How the intimate cellular interactions between inflamed cpLECs and immune cells contribute to forming an immune regulatory niche similar to autoimmune diseases described previously (Hsu et al., 2022) would need to be studied further.

The interaction of VEGF-C and VEGFR-3 has been indicated as a key driver of lymphangiogenesis (Baluk et al., 2005; Jussila and Alitalo, 2002). We showed an increase in VEGF-C near the CP after stroke induction, and additionally we identified that VEGF-C was produced by CD11b$^+$ immune cells. When lymphangiogenesis was inhibited using MAZ51, MAZ51 did not affect the sham groups, which indicates that there may be a baseline threshold in lymphatic density. Additionally, MAZ51 may inhibit recruitment and activation of immune cells. Esposito et al. (2019) observed LEC proliferation and activation of macrophages in the CLNs within 24 h after MCAO in rats. MAZ51 treatment reduced pro-inflammatory macrophages and LEC activation, which also resulted in smaller brain infarcts. They further showed that VEGF-C/VEGFR-3 interaction increased inflammatory responses in LECs in co-cultured macrophages in in vitro experiments (Esposito et al., 2019). Combined with our behavioral data showing improved locomotor ability at earlier time points, it suggests that inhibiting lymphangiogenesis with MAZ51 to reduce recruitment of activated pro-inflammatory immune cells to the brain may be beneficial at an earlier period after tMCAO.

However, Breslin et al. showed MAZ51 treatment decreased lymphatic phasic activities and function of lymphatic pumps (Breslin et al., 2007). In our study, MAZ51-treated tMCAO mice failed to show natural recovery in rotarod tests after 7 days. Interestingly, this is when we noticed a peak of lymphangiogenesis near the CP after tMCAO. As both lymphangiogenesis and lymphatic dilation were inhibited with MAZ51, the cerebral edema may further suppress other areas of the brain and induce secondary damages (Jeon et al., 2014; Wijdicks et al., 2014). Thus, it is possible that prolonged inhibition of lymphangiogenesis or lymphatic dilation may affect fluid drainage and recovery after tMCAO, but further analysis is needed to dissect the exact mechanism.

Conversely, administering VEGF-C156S directly to the brain through the CCA resulted in larger brain infarcts. VEGF-C is a chemokine regulated by infiltrating immune cells and pro-inflammatory cytokines such as IL-1β and TNF-α, unlike VEGF-A, which is mostly driven by hypoxia (Jussila and Alitalo, 2002; Enholm et al., 1997; Ristimäki et al., 1998), it is involved in not only lymphangiogenesis but also recruiting immune cells, especially those that express VEGFR-3 such as macrophages and DCs (Li et al., 2016). Thus, it is possible that VEGF-C156S resulted in increased immune cell recruitment toward core regions of brain infarcts after tMCAO which caused bigger infarcts compared with control-treated tMCAO mice. These results challenge recent reports that suggest that VEGF-C delivery after stroke may offer recovery benefits (Matta et al., 2021; Tsai et al., 2022). One explanation for this divergence in effects could be the result of differences in stroke models. Tsai et al. indicated therapeutic enhancement of meningeal lymphatics via VEGF-C156S, allowing for greater clearance of hematomas, in a model intracerebral hemorrhage not tMCAO (Tsai et al., 2022). Additionally, VEGF-C/VEGFR-3 manipulations in the pre-stroke time frame have now been conducted. Boisserand et al. demonstrated that AAV-mVEGF-C pretreatment via intra-cisterna magna (ICM) injection reduces tMCAO infarct size and leads to better post-stroke recovery (Boisserand et al., 2024). Interestingly, in the experiment by Boisserand et al., lymphatics along CSF drainage routes were primarily expanded by the ICM AAV-mVEGF-C delivery, including lymphatics in the dura, dCLN, and lower regions of the olfactory mucosa (Boisserand et al., 2024). As a result, it is possible that lymphangiogenesis in cpLVs can also be similarly induced in this ICM AAV-mVEGF-C model and mediate aspects of stroke outcome, but further investigations are needed. Similarly, AAV-mVEGF-C pretreatment via the intracerebroventricular route was shown to induce dural lymphangiogenesis and improve motor outcomes, but not reduce infarct size in tMCAO (Keuters et al., 2024). Thus beneficial manipulation of VEGF-C/VEGFR-3 signaling could be highly context dependent, unique to stroke type, stroke location, and route of therapeutic delivery. Much like current time-dependent tPA treatment protocols, there is likely a specific therapeutic window in which VEGF-C/VEGFR-3–modifying therapy might be given. There are several limitations to our study. We only investigated outcomes of up to 2 wk after tMCAO in young wild-type male mice. Long-term impacts should be investigated in aged mice. Furthermore, we should note that the VEGFR-3 inhibitor MAZ51 at higher concentrations has been shown to partially inhibit VEGFR-2 and induce apoptosis (Kirkin et al., 2001, 2004). Additionally, MAZ51 and VEGF-C were administered within a narrow window following tMCAO induction. Finally, while we investigated several relevant lymphatic regions, there are CNS-relevant lymphatic regions which we did not investigate, including the transverse dural, spinal, and several basal lymphatic structures.

In summary, this study showed that lymphatics near the CP undergo lymphangiogenesis, while dural meningeal lymphatics are dilated after tMCAO in mice. The lymphangiogenesis was driven by the interaction of VEGFR-3 and VEGF-C which is produced by myeloid cells, including DCs and macrophages. The VEGFR-3 inhibitor blocked lymphangiogenesis after tMCAO and created smaller brain infarcts. Based on the behavioral test results, inhibition of VEGFR-3–dependent lymphangiogenesis after tMCAO seems beneficial at earlier time points, but may have long-term consequences on recovery depending on the length of treatment. Administering VEGF-C into the brain directly after stroke induced bigger brain infarct areas. Together, our data suggest that VEGF-C has a dual role in stroke, with damaging impacts in the acute phase but pro-angiogenic in the chronic phase of stroke. As a result, more research is needed to investigate an optimal timing of potential VEGFR-3 and VEGF-C therapeutic manipulations, as well as more specific and safe targeting of meningeal lymphatic vessels. These data emphasize caution when targeting the VEGF-C/VEGFR-3 pathway in promoting post-stroke recovery in spite of the impressive effects of

the VEGF-C/VEGFR-3–mediated pathway on tissue regeneration following stroke.

Materials and methods

Animals

Male C57BL/6J wild type was purchased from Jackson Laboratories and housed in the University of Wisconsin at Madison Breeding Core and Research Services. Animals were kept in a pathogen-free facility with 12 h of each dark and light cycle and access to food and water. All experiments were conducted in accordance with guidelines from the National Institutes of Health and the University of Wisconsin-Madison Institutional Animal Care and Use Committee.

tMCAO

10–12-wk-old male mice (25–29 g) were used for all tMCAO surgeries. In agreement with the Stroke Therapy Academic Industry Roundtable (STAIR) criteria (Liu et al., 2009), core temperature was maintained between 36°C and 37°C during surgery with a heating pad, and post-surgery mice recovered in a temperature-controlled chamber. Mice were anesthetized using isoflurane while providing oxygen during occlusion and reperfusion surgery. During occlusion, a midline incision was made and the CCA on the right side was isolated from the vagus nerve. The external carotid artery and internal carotid artery were identified from the bifurcation of CCA. Both the bottom of the CCA and external carotid artery were permanently ligated. A temporary knot was made near the bifurcation of CCA. A microvascular clip was made on CCA, and a 6.0 nylon monofilament (602191; Doccol Corp) was inserted into the middle cerebral artery while loosening the temporary knot carefully. Temporary knot was tightened again, and the occlusion was initiated by advancing the filament ∼9–9.5 mm to block middle cerebral artery blood flow for 60 min. After 60 min, mice were anesthetized, and the filament was removed. The temporary knot was tightened as a permanent ligation. For sham mice, all surgical operations were the same, but the filament was not inserted. MRI or cresyl violet staining of stroke regions was used to verify strokes and exclude mice not presenting lesions.

Flow cytometry

After 7 days of tMCAO, single-cell suspensions from the CP were resuspended in FACS buffer (pH 7.4, 0.1 M PBS, 1 mM EDTA, and 1% BSA). Importantly, no dissociation protocol was applied to cell suspension to preserve cell–cell interactions (Giladi et al., 2020). The cells were then immunolabeled with the ghost dye UV450 dye and appropriate conjugated antibodies for 30 min at 4°C. The stained cells were washed with FACS buffer and fixed in 4% PFA (4% paraformaldehyde, 0.1 M PBS). LECs were gated as $CD45^-$, $CD31^+$, and $PDPN^+$. To identify immune cells bound to LECs, LECs were gated as $CD45^+$, $CD31^+$, and $PDPN^+$. Among LECs, DCs were gated as $CD11c^+$ and $CD11b^+$; monocytes/macrophages were gated as $CD11c^-$ and $CD11b^+$, CD4 T cells as $CD11c^-$ $CD11b^-$ and $CD4^+$, CD8 T cells as $CD11c^-$, $CD11b^-$, and $CD8^+$, and B cells as $CD11c^-$, $CD11b^-$, $CD4^-$, $CD8^-$, and $B220^+$. The data were acquired using BD LSR II Flow Cytometer (BD Biosciences) and analyzed using FlowJo software.

Histology

Mice were anesthetized with isoflurane and transcardially perfused with 1X PBS followed by 4% PFA. Then, mice were decapitated, and the whole heads without skin were fixed in 4% PFA overnight at 4°C. Then the whole heads were transferred to 14% EDTA for 7 days to decalcify followed by a cryoprotection step in 40% sucrose for 7 days at 4°C. Then, the heads were embedded in Tissue-Tek OCT Compound, frozen in dry ice, and stored at −80°C. Leica CM1800 (Leica Biosystems) cryostat was used to section each head into 60-µm tissue slides for the CP area and 30 µm for the brains and lymph nodes. Each section was mounted on Superfrost Plus microscope slides and stored at −80°C till staining.

tMCAO infarct quantification

Brain infarction was screened with a 4.7 T small animal MRI (Agilent Technologies, Inc.) and acquired with VnmrJ (Agilent Technologies) on days 3, 7, and 14. Animals were anesthetized using isoflurane through a nose cone during imaging. T2-weighted MRI scans were measured under the following parameters: repetition time (TR) = 3,500 ms, thickness = 1.0 mm, resolution = 192 × 192, and averages = 11. Each image was analyzed using FIJI software. Ischemic infarct area in percentage was calculated by dividing infarction area with total area of each brain section (both hemispheres). Infarct volume was also quantified and showed a similar trend.

Evans blue dye

Under isoflurane anesthesia using a nose cone, 10 µl of 10% Evans blue dye was injected into the cisterna magna using a Hamilton syringe at a rate of 2 µl/min. After allowing the dye to circulate for 30 min, the mouse was euthanized and the whole head was analyzed for dye distribution around the CP. MRI was done with a 4.7 T small animal MRI (Agilent Technologies, Inc.) and acquired using VnmrJ (Agilent Technologies). 2D T1-weighted MRI scans were used to detect gadolinium under the following parameters: repetition time (TR) = 688 ms, echo time (TE) = 11.26 ms, thickness = 0.5 mm, resolution = 128 × 128, and averages = 7. These resulted in a time scan of about 5 min. We repeated this scan after injection for 1 h. Animals were anesthetized using isoflurane through a nose cone and 10 ul of gadolinium was injected into the cisterna magna at a rate of 2 µl/min using a Hamilton syringe. Respiratory rates were monitored throughout the scans. A baseline scan was acquired prior to gadolinium injection with the same settings. Images were processed and analyzed using FIJI software.

IHC and confocal microscopy

For IHC, sections were rehydrated with 1X PBS for 10 min and blocking solution (1% BSA and 0.1% Triton-X in 1X PBS) for 60 min. Sections were then incubated with the appropriate primary antibodies in blocking solution at 4°C overnight in a humidified chamber. Sections were washed three times with 1X PBS for 10 min each. As necessary, sections were incubated with

the appropriate secondary antibodies at room temperature for 120 min and washed afterward. Then, each section was mounted with Prolong Gold mounting medium with DAPI, and images were acquired using an Olympus Fluoview FV1200 confocal microscope with 4×, 10×, or 20× objectives. A detailed list of reagents and antibodies is provided in Table S1.

Quantification of lymphatic morphology

Lyve-1$^+$ areas of dural lymphatics and dCLNs were calculated on FIJI software (version 2.3.0/1.53q) using the Analyze Particles functions. Z stacks of cpLVs, optic nerve, and NP were overlaid, and Lyve-1$^+$ areas were thresholded on identical settings between conditions and calculated by the Fiji measure function (Hsu et al., 2019). Lymphatic vessel loops and sprouts were counted under identical confocal settings and FIJI software (Bolte et al., 2020). Lymphatic vessel diameter was assessed with 50 random measurements per meningeal sample in each group along either COS or SSS and then averaged together. All measurements were done by an independent blinded experimenter.

Drug administration

MAZ51 was dissolved in DMSO and i.p. injected at 10 mg/kg of mouse weight on days 0 (after reperfusion of tMCAO), 2, 4, and 6. Control mice received equivalent volumes of DMSO i.p. on those same days. VEGF-C156S was dissolved in 1X PBS and 3 µg was administered through a microcatheter inserted in CCA on day 0 after reperfusion of tMCAO. Control mice received equivalent volumes of 1X PBS using the same method on day 0.

Behavior tests

Post-ischemic motor functions were measured using a rotarod (LE8205; Panlab Harvard Apparatus), ladder rung (LE780; Panlab Harvard Apparatus), and open-field test (LE802S from Panlab Harvard Apparatus). Rotarod tests were conducted for 3 min on a rotating cylinder with constant speed at 8 rpm. The ladder rung test was conducted until each mouse crossed the tapered 100-cm beam, and the number of foot faults was counted. An open-field test was used to observe spontaneous locomotor functions in a 45 (W) × 45 (D) × 40 (H)-cm box for 5 min. An open-field test was analyzed using Smart 3.0 software (Panlab Harvard Apparatus). All mice were trained with three tests 2 consecutive days before the surgery and randomized for sham or tMCAO surgery on day 0. Tests were measured on days 1, 3, 5, and 7 after MAZ51 treatment. All behavioral equipment was wiped with 70% ethanol between mice.

Statistical analysis

Sample sizes were determined according to power calculation (80% power, $\alpha = 0.05$) (Arifin and Zahiruddin, 2017; Charan and Kantharia, 2013), and age-matched mice were used for each group, with random group assignments. Statistical analysis of results was performed with GraphPad Prism 6.0 Software. When results of two groups were compared, an unpaired Student's t test was used. When results of three or more groups were compared, one-way ANOVA was used. When results were compared across different time points, two-way ANOVA with Sidak's multiple comparisons tests was used. If the same subjects were analyzed across multiple time points, two-way ANOVA with repeated measures were used with Sidak's multiple comparisons. For all statistical tests, the data are portrayed as mean ± SEM, and the significance is portrayed as: NS ($P > 0.05$), * ($P < 0.05$), ** ($P < 0.01$), *** ($P < 0.001$), **** ($P < 0.0001$).

Online supplemental material

Fig. S1 shows the analysis of lymphatic vessels at the optic nerve, NP, and dura (COS, SSS). Fig. S2 shows the localization of intracisterna magna-injected Evans blue dye at the CP of the tMCAO mouse. Fig. S3 shows the effects of MAZ51 on dura (COS, SSS) and dCLNs lymphatic vessel area during sham and post-tMCAO conditions (day 7). Fig. S4 shows the impact of MAZ51 on rotarod, foot fault, and open field tests. Fig. S5 shows the effects of immediate VEGF-C156S delivery through CCA after tMCAO on dura (COS, SSS) and dCLN lymphatic area. Loops, sprouts, and length or diameter were also quantified for CP, COS, and SSS. Table S1 presents the list of antibodies used in the study. Table S2 presents the list of reagents used in the study.

Data availability

Source data are provided with this paper. Data supporting the findings of this study are available from the corresponding authors upon reasonable request.

Acknowledgments

We thank Khen Macvilay for his expertise in flow cytometry, Laura Schmitt-Brunold for her expertise in molecular biology, and all our laboratory members for insightful comments on this work. We would like to thank the University of Wisconsin Small Animal Imaging Facility supported by the University of Wisconsin Carbone Cancer Center grant P30CA014520 to use its facilities and services.

This work was supported by the National Institutes of Health grants NS10847 and NS103506 awarded to Z. Fabry, HL128778 awarded to M. Sandor, the Neuroscience Training Program T32-GM007507 awarded to M. Hsu and C. Laaker, and American Heart Association grant 915125 awarded to C. Laaker.

Author contributions: Y.H. Choi: conceptualization, data curation, formal analysis, investigation, methodology, project administration, validation, visualization, and writing—original draft, review, and editing. M. Hsu: investigation. C. Laaker: formal analysis, investigation, visualization, and writing—original draft, review, and editing. J. Port: formal analysis and investigation. K.G. Kovács: investigation and writing—review and editing. M. Herbath: formal analysis, investigation, methodology, visualization, and writing—review and editing. H. Yang: data curation. P. Cismaru: data curation, investigation, and methodology. A.M. Johnson: investigation and writing—review and editing. B. Spellman: investigation. K. Wigand: conceptualization, formal analysis, investigation, methodology, and resources. M. Sandor: conceptualization, data curation, formal analysis, funding acquisition, project administration, resources, supervision, validation, and writing—review and editing. Z. Fabry: conceptualization, funding acquisition, methodology,

project administration, supervision, validation, visualization, and writing—review and editing.

Disclosures: The authors declare no competing interests exist.

Submitted: 5 October 2023
Revised: 25 September 2024
Accepted: 11 November 2024

References

Ahn, J.H., H. Cho, J.-H. Kim, S.H. Kim, J.-S. Ham, I. Park, S.H. Suh, S.P. Hong, J.-H. Song, Y.-K. Hong, et al. 2019. Meningeal lymphatic vessels at the skull base drain cerebrospinal fluid. *Nature*. 572:62–66. https://doi.org/10.1038/s41586-019-1419-5

Alberts, M.J. 2017. Stroke treatment with intravenous tissue-type plasminogen activator: More proof that time is brain. *Circulation*. 135:140–142. https://doi.org/10.1161/CIRCULATIONAHA.116.025724

Alitalo, K. 2011. The lymphatic vasculature in disease. *Nat. Med.* 17:1371–1380. https://doi.org/10.1038/nm.2545

Antila, S., D. Chilov, H. Nurmi, Z. Li, A. Näsi, M. Gotkiewicz, V. Sitnikova, H. Jäntti, N. Acosta, H. Koivisto, et al. 2024. Sustained meningeal lymphatic vessel atrophy or expansion does not alter Alzheimer's disease-related amyloid pathology. *Nat. Cardiovasc. Res.* 3:474–491. https://doi.org/10.1038/s44161-024-00445-9

Arifin, W.N., and W.M. Zahiruddin. 2017. Sample size calculation in animal studies using resource equation approach. *Malays. J. Med. Sci.* 24: 101–105. https://doi.org/10.21315/mjms2017.24.5.11

Aspelund, A., S. Antila, S.T. Proulx, T.V. Karlsen, S. Karaman, M. Detmar, H. Wiig, and K. Alitalo. 2015. A dural lymphatic vascular system that drains brain interstitial fluid and macromolecules. *J. Exp. Med.* 212: 991–999. https://doi.org/10.1084/jem.20142290

Aspelund, A., T. Tammela, S. Antila, H. Nurmi, V.-M. Leppänen, G. Zarkada, L. Stanczuk, M. Francois, T. Mäkinen, P. Saharinen, et al. 2014. The Schlemm's canal is a VEGF-C/VEGFR-3-responsive lymphatic-like vessel. *J. Clin. Invest.* 124:3975–3986. https://doi.org/10.1172/JCI75395

Bain, J.M., L. Moore, Z. Ren, S. Simonishvili, and S.W. Levison. 2013. Vascular endothelial growth factors A and C are induced in the SVZ following neonatal hypoxia-ischemia and exert different effects on neonatal glial progenitors. *Transl. Stroke Res.* 4:158–170. https://doi.org/10.1007/s12975-012-0213-6

Baluk, P., T. Tammela, E. Ator, N. Lyubynska, M.G. Achen, D.J. Hicklin, M. Jeltsch, T.V. Petrova, B. Pytowski, S.A. Stacker, et al. 2005. Pathogenesis of persistent lymphatic vessel hyperplasia in chronic airway inflammation. *J. Clin. Invest.* 115:247–257. https://doi.org/10.1172/JCI200522037

Barber, P.A., J. Zhang, A.M. Demchuk, M.D. Hill, and A.M. Buchan. 2001. Why are stroke patients excluded from TPA therapy? An analysis of patient eligibility. *Neurology*. 56:1015–1020. https://doi.org/10.1212/WNL.56.8.1015

Bendall, S.C. 2020. Diamonds in the doublets. *Nat. Biotechnol.* 38:559–561. https://doi.org/10.1038/s41587-020-0511-6

Boisserand, L.S.B., L.H. Geraldo, J. Bouchart, M.-R. El Kamouh, S. Lee, B.G. Sanganahalli, M. Spajer, S. Zhang, S. Lee, M. Parent, et al. 2024. VEGF-C prophylaxis favors lymphatic drainage and modulates neuroinflammation in a stroke model. *J. Exp. Med.* 221:e20221983. https://doi.org/10.1084/jem.20221983

Bolte, A.C., A.B. Dutta, M.E. Hurt, I. Smirnov, M.A. Kovacs, C.A. McKee, H.E. Ennerfelt, D. Shapiro, B.H. Nguyen, E.L. Frost, et al. 2020. Meningeal lymphatic dysfunction exacerbates traumatic brain injury pathogenesis. *Nat. Commun.* 11:4524. https://doi.org/10.1038/s41467-020-18113-4

Breslin, J.W., N. Gaudreault, K.D. Watson, R. Reynoso, S.Y. Yuan, and M.H. Wu. 2007. Vascular endothelial growth factor-C stimulates the lymphatic pump by a VEGF receptor-3-dependent mechanism. *Am. J. Physiol. Heart Circ. Physiol.* 293:H709–H718. https://doi.org/10.1152/ajpheart.00102.2007

Brogan, M.E., and E.M. Manno. 2015. Treatment of malignant brain edema and increased intracranial pressure after stroke. *Curr. Treat. Options Neurol.* 17:327. https://doi.org/10.1007/s11940-014-0327-0

Charan, J., and N.D. Kantharia. 2013. How to calculate sample size in animal studies? *J. Pharmacol. Pharmacother.* 4:303–306. https://doi.org/10.4103/0976-500X.119726

Cheng, Y.D., L. Al-Khoury, and J.A. Zivin. 2004. Neuroprotection for ischemic stroke: Two decades of success and failure. *NeuroRx*. 1:36–45. https://doi.org/10.1602/neurorx.1.1.36

Chen, J., J. He, R. Ni, Q. Yang, Y. Zhang, and L. Luo. 2019. Cerebrovascular injuries induce lymphatic invasion into brain parenchyma to guide vascular regeneration in zebrafish. *Dev. Cell*. 49:697–710.e5. https://doi.org/10.1016/j.devcel.2019.03.022

Chen, X., and K. Wang. 2016. The fate of medications evaluated for ischemic stroke pharmacotherapy over the period 1995-2015. *Acta Pharm. Sin. B.* 6:522–530. https://doi.org/10.1016/j.apsb.2016.06.013

Cserr, H.F., C.J. Harling-Berg, and P.M. Knopf. 1992. Drainage of brain extracellular fluid into blood and deep cervical lymph and its immunological significance. *Brain Pathol.* 2:269–276. https://doi.org/10.1111/j.1750-3639.1992.tb00703.x

Da Mesquita, S., A. Louveau, A. Vaccari, I. Smirnov, R.C. Cornelison, K.M. Kingsmore, C. Contarino, S. Onengut-Gumuscu, E. Farber, D. Raper, et al. 2018. Functional aspects of meningeal lymphatics in ageing and Alzheimer's disease. *Nature*. 560:185–191. https://doi.org/10.1038/s41586-018-0368-8

D'Mello, C., T. Le, and M.G. Swain. 2009. Cerebral microglia recruit monocytes into the brain in response to tumor necrosis factoralpha signaling during peripheral organ inflammation. *J. Neurosci.* 29:2089–2102. https://doi.org/10.1523/JNEUROSCI.3567-08.2009

Dostovic, Z., E. Dostovic, D. Smajlovic, O.C. Ibrahimagic, and L. Avdic. 2016. Brain edema after ischaemic stroke. *Med. Arch.* 70:339–341. https://doi.org/10.5455/medarh.2016.70.339-341

Engelhardt, B., P. Vajkoczy, and R.O. Weller. 2017. The movers and shapers in immune privilege of the CNS. *Nat. Immunol.* 18:123–131. https://doi.org/10.1038/ni.3666

Enholm, B., K. Paavonen, A. Ristimäki, V. Kumar, Y. Gunji, J. Klefstrom, L. Kivinen, M. Laiho, B. Olofsson, V. Joukov, et al. 1997. Comparison of VEGF, VEGF-B, VEGF-C and Ang-1 mRNA regulation by serum, growth factors, oncoproteins and hypoxia. *Oncogene*. 14:2475–2483. https://doi.org/10.1038/sj.onc.1201090

Esposito, E., B.J. Ahn, J. Shi, Y. Nakamura, J.H. Park, E.T. Mandeville, Z. Yu, S.J. Chan, R. Desai, A. Hayakawa, et al. 2019. Brain-to-cervical lymph node signaling after stroke. *Nat. Commun.* 10:5306. https://doi.org/10.1038/s41467-019-13324-w

Flister, M.J., A. Wilber, K.L. Hall, C. Iwata, K. Miyazono, R.E. Nisato, M.S. Pepper, D.C. Zawieja, and S. Ran. 2010. Inflammation induces lymphangiogenesis through up-regulation of VEGFR-3 mediated by NF-kappaB and Prox1. *Blood*. 115:418–429. https://doi.org/10.1182/blood-2008-12-196840

Gesuete, R., S.L. Stevens, and M.P. Stenzel-Poore. 2016. Role of circulating immune cells in stroke and preconditioning-induced protection. *Acta Neurochir. Suppl.* 121:39–44. https://doi.org/10.1007/978-3-319-18497-5_7

Giladi, A., M. Cohen, C. Medaglia, Y. Baran, B. Li, M. Zada, P. Bost, R. Blecher-Gonen, T.-M. Salame, J.U. Mayer, et al. 2020. Dissecting cellular crosstalk by sequencing physically interacting cells. *Nat. Biotechnol.* 38: 629–637. https://doi.org/10.1038/s41587-020-0442-2

Gravanis, I., and S.E. Tsirka. 2008. Tissue-type plasminogen activator as a therapeutic target in stroke. *Expert Opin. Ther. Targets*. 12:159–170. https://doi.org/10.1517/14728222.12.2.159

Gu, W., T. Brännström, W. Jiang, A. Bergh, and P. Wester. 2001. Vascular endothelial growth factor-A and -C protein up-regulation and early angiogenesis in a rat photothrombotic ring stroke model with spontaneous reperfusion. *Acta Neuropathol.* 102:216–226. https://doi.org/10.1007/s004010100370

Halpern, K.B., R. Shenhav, H. Massalha, B. Toth, A. Egozi, E.E. Massasa, C. Medgalia, E. David, A. Giladi, A.E. Moor, et al. 2018. Paired-cell sequencing enables spatial gene expression mapping of liver endothelial cells. *Nat. Biotechnol.* 36:962–970. https://doi.org/10.1038/nbt.4231

Hsu, M., C. Laaker, A. Madrid, M. Herbath, Y.H. Choi, M. Sandor, and Z. Fabry. 2022. Neuroinflammation creates an immune regulatory niche at the meningeal lymphatic vasculature near the cribriform plate. *Nat. Immunol.* 23:581–593. https://doi.org/10.1038/s41590-022-01158-6

Hsu, M., A. Rayasam, J.A. Kijak, Y.H. Choi, J.S. Harding, S.A. Marcus, W.J. Karpus, M. Sandor, and Z. Fabry. 2019. Neuroinflammation-induced lymphangiogenesis near the cribriform plate contributes to drainage of CNS-derived antigens and immune cells. *Nat. Commun.* 10:229. https://doi.org/10.1038/s41467-018-08163-0

Hu, X., Q. Deng, L. Ma, Q. Li, Y. Chen, Y. Liao, F. Zhou, C. Zhang, L. Shao, J. Feng, et al. 2020. Meningeal lymphatic vessels regulate brain tumor drainage and immunity. *Cell Res.* 30:229–243. https://doi.org/10.1038/s41422-020-0287-8

Jeon, S.-B., Y. Koh, H.A. Choi, and K. Lee. 2014. Critical care for patients with massive ischemic stroke. *J. Stroke*. 16:146–160. https://doi.org/10.5853/jos.2014.16.3.146

Joukov, V., V. Kumar, T. Sorsa, E. Arighi, H. Weich, O. Saksela, and K. Alitalo. 1998. A recombinant mutant vascular endothelial growth factor-C that has lost vascular endothelial growth factor receptor-2 binding, activation, and vascular permeability activities. *J. Biol. Chem.* 273:6599–6602. https://doi.org/10.1074/jbc.273.12.6599

Jussila, L., and K. Alitalo. 2002. Vascular growth factors and lymphangiogenesis. *Physiol. Rev.* 82:673–700. https://doi.org/10.1152/physrev.00005.2002

Kajiya, K., M. Sawane, R. Huggenberger, and M. Detmar. 2009. Activation of the VEGFR-3 pathway by VEGF-C attenuates UVB-induced edema formation and skin inflammation by promoting lymphangiogenesis. *J. Invest. Dermatol.* 129:1292–1298. https://doi.org/10.1038/jid.2008.351

Keuters, M.H., S. Antila, R. Immonen, L. Plotnikova, S. Wojciechowski, S. Lehtonen, K. Alitalo, J. Koistinaho, and H. Dhungana. 2024. The impact of VEGF-C-induced Dural lymphatic vessel growth on ischemic stroke pathology. *Transl. Stroke Res.* https://doi.org/10.1007/s12975-024-01262-9

Kim, I.-D., J.W. Cave, and S. Cho. 2021. Aflibercept, a VEGF (vascular endothelial growth factor)-trap, reduces vascular permeability and stroke-induced brain swelling in obese mice. *Stroke*. 52:2637–2648. https://doi.org/10.1161/STROKEAHA.121.034362

Kim, J.S. 2019. tPA helpers in the treatment of acute ischemic stroke: Are they ready for clinical use? *J. Stroke*. 21:160–174. https://doi.org/10.5853/jos.2019.00584

Kirkin, V., R. Mazitschek, J. Krishnan, A. Steffen, J. Waltenberger, M.S. Pepper, A. Giannis, and J.P. Sleeman. 2001. Characterization of indolinones which preferentially inhibit VEGF-C- and VEGF-D-induced activation of VEGFR-3 rather than VEGFR-2. *Eur. J. Biochem.* 268:5530–5540. https://doi.org/10.1046/j.1432-1033.2001.02476.x

Kirkin, V., W. Thiele, P. Baumann, R. Mazitschek, K. Rohde, G. Fellbrich, H. Weich, J. Waltenberger, A. Giannis, and J.P. Sleeman. 2004. MAZ51, an indolinone that inhibits endothelial cell and tumor cell growth in vitro, suppresses tumor growth in vivo. *Int. J. Cancer*. 112:986–993. https://doi.org/10.1002/ijc.20509

Knecht, T., C. Borlongan, and I. Dela Peña. 2018. Combination therapy for ischemic stroke: Novel approaches to lengthen therapeutic window of tissue plasminogen activator. *Brain Circ.* 4:99–108. https://doi.org/10.4103/bc.bc_21_18

Knecht, T., J. Story, J. Liu, W. Davis, C.V. Borlongan, and I.C. Dela Peña. 2017. Adjunctive therapy approaches for ischemic stroke: Innovations to expand time window of treatment. *Int. J. Mol. Sci.* 18:2756. https://doi.org/10.3390/ijms18122756

Laaker, C., C. Baenen, K.G. Kovács, M. Sandor, and Z. Fabry. 2023. Immune cells as messengers from the CNS to the periphery: The role of the meningeal lymphatic system in immune cell migration from the CNS. *Front. Immunol.* 14:1233908. https://doi.org/10.3389/fimmu.2023.1233908

Lin, Z.-J., H.-Y. Qiu, X.-X. Tong, Y. Guo, M.-F. Han, C.-S. Yang, K.-H. Lin, J. Wu, X. Li, and Y. Yang. 2018. Evaluation of efficacy and safety of Reteplase and Alteplase in the treatment of hyper-acute cerebral infarction. *Biosci. Rep.* 38:BSR20170730. https://doi.org/10.1042/BSR20170730

Liu, S., G. Zhen, B.P. Meloni, K. Campbell, and H.R. Winn. 2009. Rodent stroke model guidelines for preclinical stroke trials (1st edition). *J. Exp. Stroke Transl. Med.* 2:2–27. https://doi.org/10.6030/1939-067X-2.2.2

Li, Y.-L., H. Zhao, and X.-B. Ren. 2016. Relationship of VEGF/VEGFR with immune and cancer cells: Staggering or forward? *Cancer Biol. Med.* 13:206–214. https://doi.org/10.20892/j.issn.2095-3941.2015.0070

Madarasz, A., L. Xin, and S.T. Proulx. 2024. Clearance of erythrocytes from the subarachnoid space through cribriform plate lymphatics in female mice. *EBioMedicine*. 107:105295. https://doi.org/10.1016/j.ebiom.2024.105295

Ma, Q., B.V. Ineichen, M. Detmar, and S.T. Proulx. 2017. Outflow of cerebrospinal fluid is predominantly through lymphatic vessels and is reduced in aged mice. *Nat. Commun.* 8:1434. https://doi.org/10.1038/s41467-017-01484-6

Matta, R., Y. Feng, L.H. Sansing, and A.L. Gonzalez. 2021. Endothelial cell secreted VEGF-C enhances NSC VEGFR3 expression and promotes NSC survival. *Stem Cell Res.* 53:102318. https://doi.org/10.1016/j.scr.2021.102318

Melin, E., P.K. Eide, and G. Ringstad. 2020. In vivo assessment of cerebrospinal fluid efflux to nasal mucosa in humans. *Sci. Rep.* 10:14974. https://doi.org/10.1038/s41598-020-72031-5

Miller, D.J., J.R. Simpson, and B. Silver. 2011. Safety of thrombolysis in acute ischemic stroke: A review of complications, risk factors, and newer technologies. *Neurohospitalist*. 1:138–147. https://doi.org/10.1177/1941875211408731

Mollanji, R., R. Bozanovic-Sosic, I. Silver, B. Li, C. Kim, R. Midha, and M. Johnston. 2001. Intracranial pressure accommodation is impaired by blocking pathways leading to extracranial lymphatics. *Am. J. Physiol. Regul. Integr. Comp. Physiol.* 280:R1573–R1581. https://doi.org/10.1152/ajpregu.2001.280.5.R1573

Özlüer, Y.E., and M. Avcil. 2017. Providing full recovery with single-dose intravenous reteplase in a patient presented to emergency department with acute ischemic stroke. *Clin. Case Rep.* 5:598–600. https://doi.org/10.1002/ccr3.895

Pashenkov, M., N. Teleshova, and H. Link. 2003. Inflammation in the central nervous system: The role for dendritic cells. *Brain Pathol.* 13:23–33. https://doi.org/10.1111/j.1750-3639.2003.tb00003.x

Petrova, T.V., and G.Y. Koh. 2020. Biological functions of lymphatic vessels. *Science*. 369:eaax4063. https://doi.org/10.1126/science.aax4063

Proulx, S.T. 2021. Cerebrospinal fluid outflow: A review of the historical and contemporary evidence for arachnoid villi, perineural routes, and dural lymphatics. *Cell. Mol. Life Sci.* 78:2429–2457. https://doi.org/10.1007/s00018-020-03706-5

Ristimäki, A., K. Narko, B. Enholm, V. Joukov, and K. Alitalo. 1998. Proinflammatory cytokines regulate expression of the lymphatic endothelial mitogen vascular endothelial growth factor-C. *J. Biol. Chem.* 273:8413–8418. https://doi.org/10.1074/jbc.273.14.8413

Rosenberg, G.A. 1999. Ischemic brain edema. *Prog. Cardiovasc. Dis.* 42:209–216. https://doi.org/10.1016/S0033-0620(99)70003-4

Ruan, J., and Y. Yao. 2020. Behavioral tests in rodent models of stroke. *Brain Hemorrhages*. 1:171–184. https://doi.org/10.1016/j.hest.2020.09.001

Rutkowski, J.M., M. Moya, J. Johannes, J. Goldman, and M.A. Swartz. 2006. Secondary lymphedema in the mouse tail: Lymphatic hyperplasia, VEGF-C upregulation, and the protective role of MMP-9. *Microvasc. Res.* 72:161–171. https://doi.org/10.1016/j.mvr.2006.05.009

Schulz, M., and B. Engelhardt. 2005. The circumventricular organs participate in the immunopathogenesis of experimental autoimmune encephalomyelitis. *Cerebrospinal Fluid Res.* 2:8. https://doi.org/10.1186/1743-8454-2-8

Shin, Y.-J., J.-S. Choi, J.-Y. Lee, J.-Y. Choi, J.-H. Cha, M.-H. Chun, and M.-Y. Lee. 2008. Differential regulation of vascular endothelial growth factor-C and its receptor in the rat hippocampus following transient forebrain ischemia. *Acta Neuropathol.* 116:517–527. https://doi.org/10.1007/s00401-008-0423-x

Si, J., L. Chen, and Z. Xia. 2006. Effects of cervical-lymphatic blockade on brain edema and infarction volume in cerebral ischemic rats. *Chin. J. Physiol.* 49:258–265.

Skillings, E.A., N.I. Wood, and A.J. Morton. 2014. Beneficial effects of environmental enrichment and food entrainment in the R6/2 mouse model of Huntington's disease. *Brain Behav.* 4:675–686. https://doi.org/10.1002/brb3.235

Spera, I., N. Cousin, M. Ries, A. Kedracka, A. Castillo, S. Aleandri, M. Vladymyrov, J.A. Mapunda, B. Engelhardt, P. Luciani, et al. 2023. Open pathways for cerebrospinal fluid outflow at the cribriform plate along the olfactory nerves. *EBioMedicine*. 91:104558. https://doi.org/10.1016/j.ebiom.2023.104558

Stroke Therapy Academic Industry Roundtable II (STAIR-II). 2001. Recommendations for clinical trial evaluation of acute stroke therapies. *Stroke*. 32:1598–1606. https://doi.org/10.1161/01.STR.32.7.1598

Thorén, M., E. Azevedo, J. Dawson, J.A. Egido, A. Falcou, G.A. Ford, S. Holmin, R. Mikulik, J. Ollikainen, N. Wahlgren, and N. Ahmed. 2017. Predictors for cerebral edema in acute ischemic stroke treated with intravenous thrombolysis. *Stroke*. 48:2464–2471. https://doi.org/10.1161/STROKEAHA.117.018223

Tsai, H.-H., Y.-C. Hsieh, J.S. Lin, Z.-T. Kuo, C.-Y. Ho, C.-H. Chen, and C.-F. Chang. 2022. Functional investigation of meningeal lymphatic system in experimental intracerebral hemorrhage. *Stroke*. 53:987–998. https://doi.org/10.1161/STROKEAHA.121.037834

Virani, S.S., A. Alonso, E.J. Benjamin, M.S. Bittencourt, C.W. Callaway, A.P. Carson, A.M. Chamberlain, A.R. Chang, S. Cheng, F.N. Delling, et al. 2020. Heart disease and stroke statistics-2020 update: A report from the American Heart association. *Circulation*. 141:e139–e596. https://doi.org/10.1161/CIR.0000000000000757

Walter, B.A., V.A. Valera, S. Takahashi, and T. Ushiki. 2006. The olfactory route for cerebrospinal fluid drainage into the peripheral lymphatic system. *Neuropathol. Appl. Neurobiol.* 32:388–396. https://doi.org/10.1111/j.1365-2990.2006.00737.x

Wen, Y.-R., J.-H. Yang, X. Wang, and Z.-B. Yao. 2018. Induced dural lymphangiogenesis facilities soluble amyloid-beta clearance from brain in a

transgenic mouse model of Alzheimer's disease. *Neural Regen. Res.* 13: 709–716. https://doi.org/10.4103/1673-5374.230299

Wijdicks, E.F.M., K.N. Sheth, B.S. Carter, D.M. Greer, S.E. Kasner, W.T. Kimberly, S. Schwab, E.E. Smith, R.J. Tamargo, M. Wintermark, and American Heart Association Stroke Council. 2014. Recommendations for the management of cerebral and cerebellar infarction with swelling: A statement for healthcare professionals from the American Heart association/American stroke association. *Stroke*. 45:1222–1238. https://doi.org/10.1161/01.str.0000441965.15164.d6

Xu, S.-Y., and S.-Y. Pan. 2013. The failure of animal models of neuroprotection in acute ischemic stroke to translate to clinical efficacy. *Med. Sci. Monit. Basic Res.* 19:37–45. https://doi.org/10.12659/MSMBR.883750

Yanev, P., K. Poinsatte, D. Hominick, N. Khurana, K.R. Zuurbier, M. Berndt, E.J. Plautz, M.T. Dellinger, and A.M. Stowe. 2020. Impaired meningeal lymphatic vessel development worsens stroke outcome. *J. Cereb. Blood Flow Metab.* 40:263–275. https://doi.org/10.1177/0271678X18822921

Yan, H., C. Zhang, Z. Wang, T. Tu, H. Duan, Y. Luo, J. Feng, F. Liu, and X. Yan. 2017. CD146 is required for VEGF-C-induced lymphatic sprouting during lymphangiogenesis. *Sci. Rep.* 7:7442. https://doi.org/10.1038/s41598-017-06637-7

Yoon, J.-H., H. Jin, H.J. Kim, S.P. Hong, M.J. Yang, J.H. Ahn, Y.-C. Kim, J. Seo, Y. Lee, D.M. McDonald, et al. 2024. Nasopharyngeal lymphatic plexus is a hub for cerebrospinal fluid drainage. *Nature*. 625:768–777. https://doi.org/10.1038/s41586-023-06899-4

Zhou, Y., W. Ran, Z. Luo, J. Wang, M. Fang, K. Wei, J. Sun, and M. Lou. 2022. Impaired peri-olfactory cerebrospinal fluid clearance is associated with ageing, cognitive decline and dyssomnia. *EBioMedicine*. 86:104381. https://doi.org/10.1016/j.ebiom.2022.104381

JEM

Supplemental material

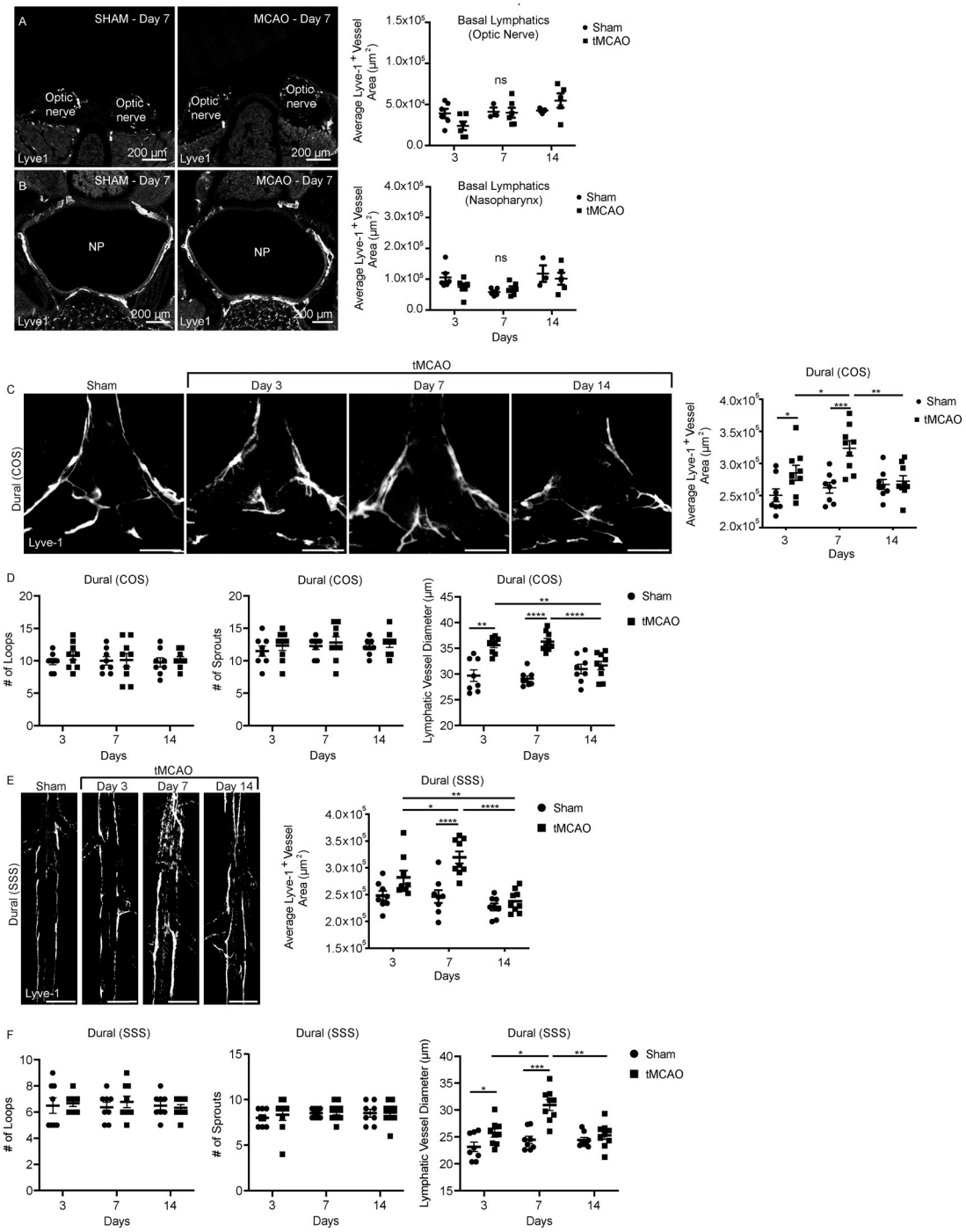

Figure S1. **Lymphatic analysis of optic nerve, NP, and dura. (A)** Coronal sections of optic nerve regions were stained with Lyve-1 fluorescent antibody in either control or tMCAO mice at days 3, 7, and 14. Representative confocal images of Lyve-1$^+$ regions near the optic nerve. Quantitation of each image (n = 3–6 mice per group; mean ± SEM, two-way ANOVA). Scale bars = 200 µm. **(B)** Coronal sections of NP regions were stained with Lyve-1 fluorescent antibody in either control or tMCAO mice at days 3, 7, and 14. Representative confocal images of Lyve-1$^+$ regions surrounding the NP. Quantitation of each image (n = 3–6 mice per group; mean ± SEM, two-way ANOVA). Scale bars = 200 µm. **(C)** COS of dural lymphatic vessels was stained with Lyve-1 antibody and imaged using confocal microscopy after sham and tMCAO at days 3, 7, and 14. Representative confocal images of COS. Scale bars = 500 µm. Quantitation of average Lyve-1$^+$ vessel areas in the COS (n = 8 mice for sham, n = 9 mice for tMCAO; mean ± SEM, *P ≤ 0.05, **P ≤ 0.01, ***P ≤ 0.001, two-way ANOVA). **(D)** Quantitation of number of loops, number of sprouts, and lymphatic vessel diameters of COS of dural lymphatic vessels after sham and tMCAO at days 3, 7, and 14 (n = 8 mice for sham, n = 9 mice for tMCAO; mean ± SEM, **P ≤ 0.01, ****P ≤ 0.0001, two-way ANOVA). **(E)** SSS of dural lymphatic vessels was immunolabeled with Lyve-1 fluorescent antibody and imaged after sham and tMCAO at days 3, 7, and 14. Representative confocal images of SSS. Quantitation of average Lyve-1$^+$ vessel areas in the SSS (n = 8 mice for sham, n = 9 mice for tMCAO; mean ± SEM, *P ≤ 0.05, **P ≤ 0.01, ****P ≤ 0.0001, two-way ANOVA). Scale bars = 500 µm. **(F)** Quantitation of number of loops, number of sprouts, and lymphatic vessel diameters of SSS of dural lymphatic vessels after sham and tMCAO at days 3, 7, and 14 (n = 8 mice for sham, n = 9 mice for tMCAO; mean ± SEM, *P ≤ 0.05, **P ≤ 0.01, ***P ≤ 0.001, two-way ANOVA). Source data are available for this figure: SourceData FS1.

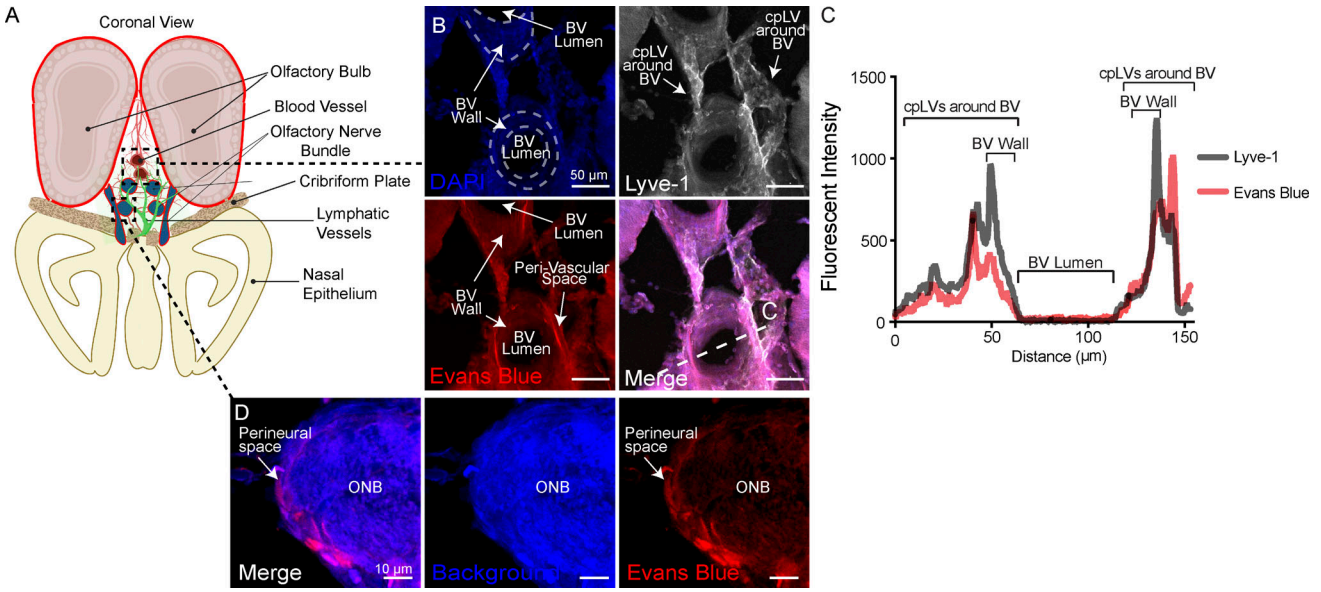

Figure S2. **CP lymphatic vessels and the perineural space of olfactory nerves can drain CSF after tMCAO. (A)** Cartoon schematic of coronally sectioned OB/CP region. Note the cpLVs interface with both BV and ONB (created using https://BioRender.com). **(B)** After 7 days of tMCAO, 10% Evans blue dye was injected into the cisterna magna (30 min) to confirm CSF drainage through lymphatics near the CP. Representative confocal images show overlap of Evans blue dye and Lyve-1 which interfaces with BV. Scale bars = 50 µm. **(C)** The intensity profile plot shows co-localization of Evans blue dye within Lyve-1⁺ cpLVs. No dye was detected in the lumen of BV, only in the Lyve-1⁺ perivascular space. **(D)** Evans blue injected into the cisterna magna accumulates around ONB at the CP at day 7 of tMCAO. Confocal images show perineural accumulation after tMCAO. Scale bars = 10 µm. BV = blood vessels, ONB = olfactory nerve bundles. Source data are available for this figure: SourceData FS2.

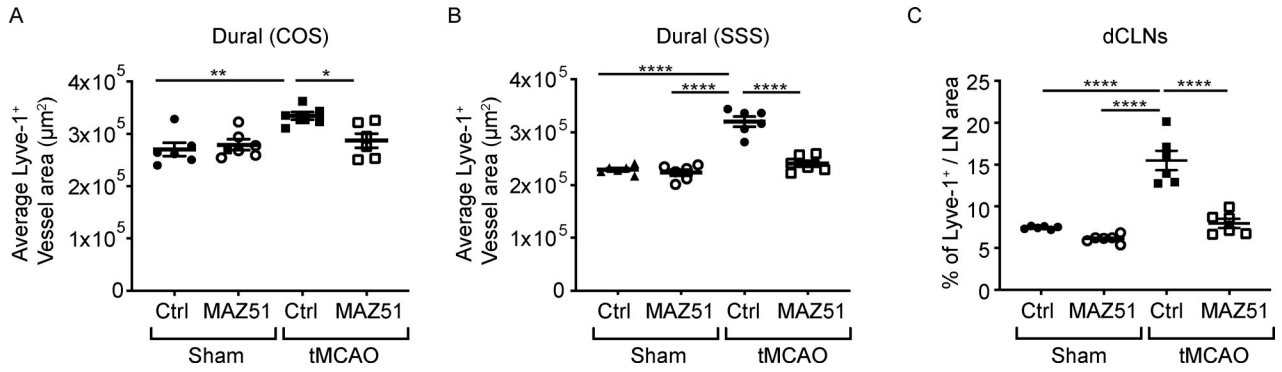

Figure S3. **MAZ51 reduces post-stroke dural and cervical lymph node lymphatic vessel area. (A and B)** Quantitation of average Lyve-1⁺ vessel area near the COS (A) and SSS (B) of dural lymphatic vessels after either control or MAZ51 treatments between sham and tMCAO (n = 6 mice per group; mean ± SEM, *P ≤ 0.05, **P ≤ 0.01, ****P ≤ 0.0001, one-way ANOVA). **(C)** Quantitation of average Lyve-1⁺ vessel area within dCLNs. (n = 6 mice per group; mean ± SEM, ****P ≤ 0.0001, one-way ANOVA). Source data are available for this figure: SourceData FS3.

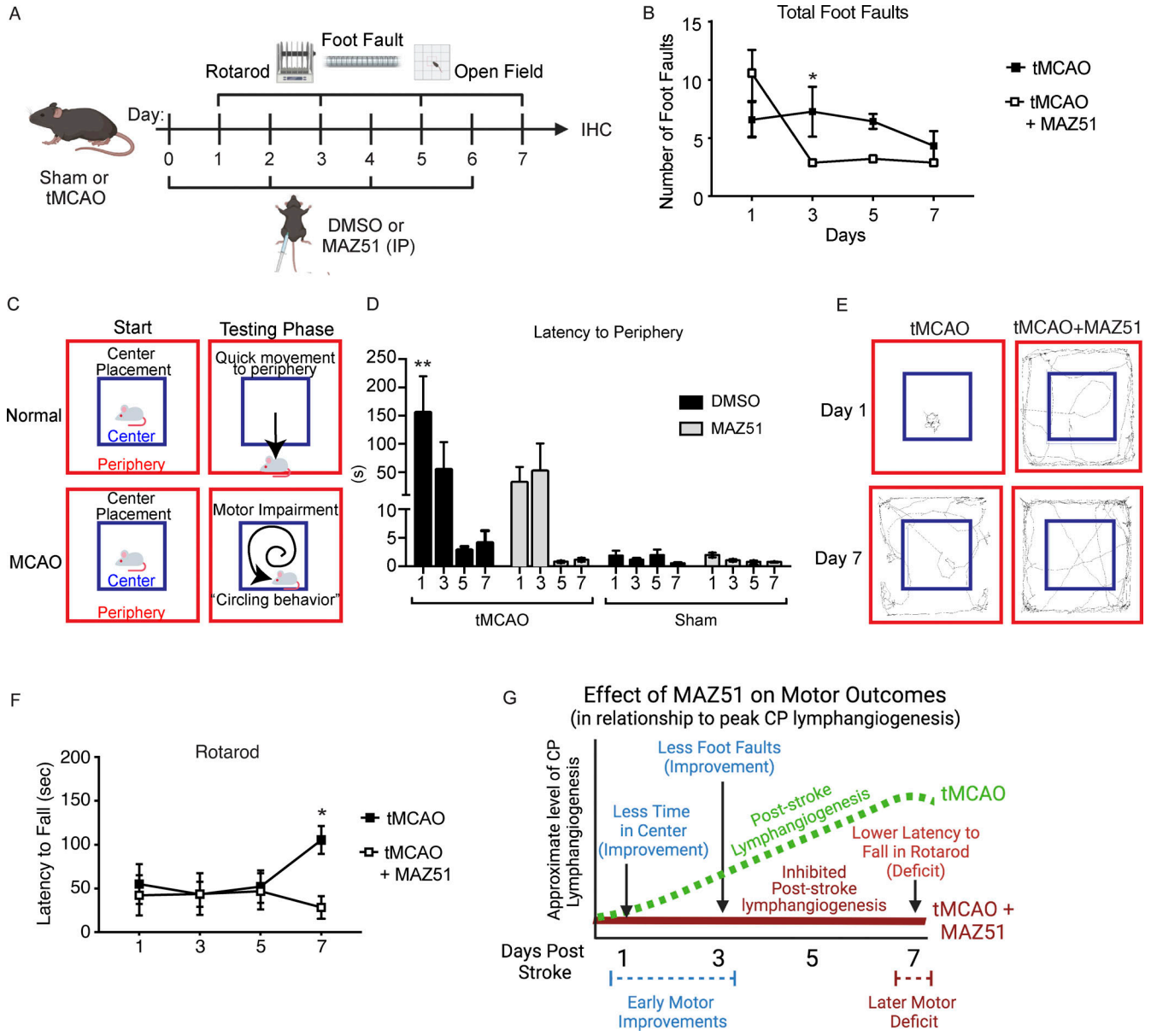

Figure S4. **MAZ51 improves early post-stroke motor outcomes. (A)** Experimental timeline of behavioral analysis in MAZ51-treated tMCAO mice (i.p. injected on days 0, 2, 4, and 6). Mice were tested in rotarod, open field, and foot fault for post-stroke motor function across days 1, 3, 5, and 7 (created using https://BioRender.com). **(B)** The ladder rung test was used to measure the total number of foot faults to assess locomotor ability between control-treated tMCAO mice and MAZ51-treated tMCAO mice at days 1, 3, 5, and 7 (n = 6 mice per group; mean ± SEM, *P < 0.05, two-way ANOVA with repeated measures and Sidak's multiple comparison test). **(C)** An open-field behavioral test was used to track the ability of the mouse to move to the peripheral wall after initial placement. Healthy/sham mice within seconds move to the peripheral wall. tMCAO mice have difficulty moving in a straight line due to single-side paralysis/circling behavior and have elevated time to reach the periphery. **(D)** Latency to reach the periphery of the open-field box was measured between all groups, including control-treated tMCAO mice and MAZ51-treated tMCAO mice, at days 1, 3, 5, and 7 (n = 6 mice per group; mean ± SEM, **P ≤ 0.05, two-way ANOVA with repeated measures and Sidak's multiple comparison test). **(E)** Representative track maps between tMCAO with control or MAZ51 at days 1 and 7 for comparison. The blue box indicates the center of the box and the red line indicates the peripheral boundary of the box. While control-treated tMCAO mice showed difficulties in movement, MAZ51-treated tMCAO mice showed improved locomotor activities at day 1. **(F)** Latency duration on the rotarod was measured between control-treated tMCAO mice and MAZ51-treated tMCAO mice at days 1, 3, 5, and 7 (n = 6 mice per group; mean ± SEM, *P < 0.05, two-way ANOVA with repeated measures and Sidak's multiple comparison test). **(G)** Timeline summary of motor function effects of MAZ51 treatment in relation to relative peak CP lymphangiogenesis (day 7). Early improvements in motor recovery (days 1–3), but late deficit in rotarod (day 7) could be associated with sustained MAZ51 inhibition of lymphangiogenesis. Peak post-stroke lymphangiogenesis typically occurs at the CP on day 7 after stroke (created using https://BioRender.com). Source data are available for this figure: SourceData FS4.

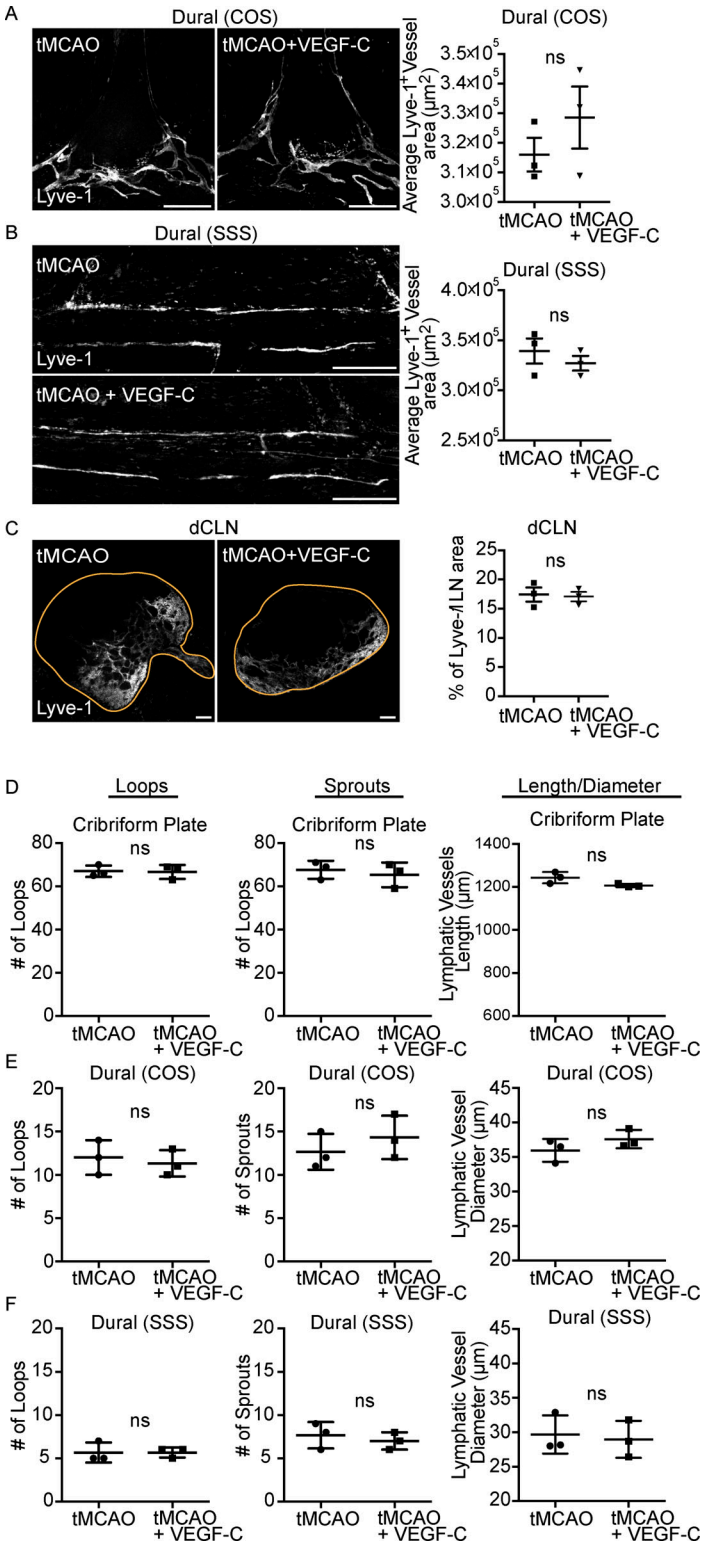

Figure S5. **VEGF-C156S delivery through the CCA immediately after tMCAO does not influence lymphatic vessel area at COS, SSS, and dCLN. (A–C)** IHC sections of COS of dural lymphatic vessels (A), SSS of dural lymphatic vessels (B), and sections of dCLN (C) were stained with Lyve-1 fluorescent antibody after either control or VEGF-C156S treatment of tMCAO mice. Representative confocal images of lymphatic vessels near COS and SSS of dura and dCLN. Quantitation of each image (n = 3 mice per group; mean ± SEM, unpaired Student's t test). Scale bars = 500 μm for COS and SSS of dural lymphatic vessels and 100 μm for dCLN. **(D)** Quantitation of number of loops, sprouts, and vessel length near the cribriform in untreated and VEGF-C–treated tMCAO mice at day 7 (n = 3 mice per group; mean ± SEM, unpaired Student's t test). **(E)** Quantitation of number of loops, sprouts, and lymphatic vessel diameter near the dural COS in untreated and VEGF-C–treated tMCAO mice at day 7 (n = 3 mice per group; mean ± SEM, unpaired Student's t test). **(F)** Quantitation of number of loops, sprouts, and lymphatic vessel diameter near the dural SSS in untreated and VEGF-C–treated tMCAO mice at day 7 (n = 3 mice per group; mean ± SEM, unpaired Student's t test). Source data are available for this figure: SourceData FS5.

Provided online are Table S1 and Table S2. Table S1 shows the antibody list. Table S2 shows the reagent list.